JCB Journal of Cell Biology

ARTICLE

DAPLE orchestrates apical actomyosin assembly from junctional polarity complexes

Arthur Marivin[1], Rachel Xi-Yeen Ho[1], and Mikel Garcia-Marcos[1]

Establishment of apicobasal polarity and the organization of the cytoskeleton must operate coordinately to ensure proper epithelial cell shape and function. However, the precise molecular mechanisms by which polarity complexes directly instruct the cytoskeletal machinery to determine cell shape are poorly understood. Here, we define a mechanism by which the PAR polarity complex (PAR3–PAR6–aPKC) at apical cell junctions leads to efficient assembly of the apical actomyosin network to maintain epithelial cell morphology. We found that the PAR polarity complex recruits the protein DAPLE to apical cell junctions, which in turn triggers a two-pronged mechanism that converges upon assembly of apical actomyosin. More specifically, DAPLE directly recruits the actin-stabilizing protein CD2AP to apical junctions and, concomitantly, activates heterotrimeric G protein signaling in a GPCR-independent manner to favor RhoA-myosin activation. These observations establish DAPLE as a direct molecular link between junctional polarity complexes and the formation of apical cytoskeletal assemblies that support epithelial cell shape.

Introduction

Epithelial cells rely on a contractile actomyosin network at their apical cortex for maintaining shape and function. This network consists of actin fibers (F-actin) crosslinked with myosin motors, which, together, generate contractile forces. The apical actomyosin network is connected to apical cell junctions, which serve not only as physical connectors of contractile cortices across cells, but also as critical regulators of the contractile machinery itself (Lecuit et al., 2011; Siedlik and Nelson, 2015; Takeichi, 2014). Mounting evidence indicates that apical junctions are organizing hubs that recruit factors for the formation and stabilization of apical F-actin and for the activation of myosin II (Charras and Yap, 2018; Yano et al., 2017; Zihni et al., 2016). Notably, activation of RhoA signaling at junctions contributes to actin assembly through mDia (Acharya et al., 2017; Carramusa et al., 2007), and other formins (Chesarone et al., 2010) and to myosin II activation through Rho-associated protein kinase (ROCK)–mediated phosphorylation (Ratheesh et al., 2012; Terry et al., 2011), leading to the subsequent increase in contractility. Thus, apical junctions integrate cell–cell adhesion and contractility by directly anchoring the same apical actin cables whose formation and stabilization they contribute to, and by activating the myosin II motors that pull from these cables to generate forces. Moreover, an emergent concept is that forces on apical junctions create biomechanical feedback that tunes the biochemical mechanisms controlling contractility (Choi et al., 2016; Gilmour et al., 2017; Lecuit and Yap, 2015; Yu and Zallen, 2020). This makes apical junctions active players in the many processes in which the interplay between cell–cell adhesion and contractility are crucial, from the dynamic morphogenetic processes that shape epithelial tissues during development (Gilmour et al., 2017; Harris and Peifer, 2004; Lecuit et al., 2011) and regeneration (Kim et al., 2020), to the maintenance of tissue integrity (Acharya et al., 2017; Kannan and Tang, 2018; Tang, 2018) and barrier function (Choi et al., 2016; Marchiando et al., 2010; Yano et al., 2017) under homeostatic tension.

Apical cell junctions are also critical to define epithelial apicobasal polarity. Polarity of epithelial cells is essential for their function, and it is closely intertwined with the cytoskeletal machinery that mediates the acquisition and maintenance of cell shape (Chen and Macara, 2005; Kuchinke et al., 1998; Nance and Zallen, 2011; Rodriguez-Boulan and Macara, 2014). The epithelial cell polarity program is controlled by protein assemblies, known as polarity complexes, that regulate each other reciprocally to maintain the identity and function of different cellular subcompartments (apical, basolateral, and basal; Rodriguez-Boulan and Macara, 2014). Thus, apical junctions are not mere physical

[1]Department of Biochemistry, Boston University School of Medicine, Boston, MA.

Correspondence to Mikel Garcia-Marcos: mgm1@bu.edu; Arthur Marivin: amarivin@bu.edu

Rachel Xi-Yeen Ho's present address is Department of Pharmacology and Experimental Therapeutics, Boston University School of Medicine, Boston, MA.

boundaries that separate the apical membrane domain from basolateral membranes. Rather, they are the sites from which polarity complexes like the PAR polarity complex, which is composed of PAR3, PAR6, and aPKC, operate (Chen and Macara, 2005; Lin et al., 2000; Suzuki and Ohno, 2006). The localization of PAR3, the primary scaffold of this complex, whose localization is restricted to apical junctions upon association with and regulation by the PAR6-aPKC module (Morais-de-Sa et al., 2010; Nagai-Tamai et al., 2002; Suzuki et al., 2001). While PAR3 and the PAR polarity complex have been shown to regulate RhoA-mediated remodeling of the apical actomyosin network in epithelia (Chen and Macara, 2005; David et al., 2010; Harris and Peifer, 2004; Muller and Wieschaus, 1996; Nance and Zallen, 2011; Silver et al., 2019; Zallen and Wieschaus, 2004), the precise molecular mechanisms involved remain ill defined.

Increasing evidence has implicated heterotrimeric G proteins (Gαβγ), the GTPases that are typically activated by G protein–coupled receptors (GPCRs), in the regulation of apical actomyosin (Bailles et al., 2019; Costa et al., 1994; Jha et al., 2018; Kanesaki et al., 2013; Kerridge et al., 2016; Manning et al., 2013; Manning and Rogers, 2014; Parks and Wieschaus, 1991). A recent study described a RhoA-dependent actomyosin activation mechanism at apical cell junctions that is mediated by heterotrimeric G protein–stimulated p114RhoGEF (Acharya et al., 2018), a Rho guanine nucleotide exchange factor (RhoGEF) that specifically localizes at apical junctions (Nakajima and Tanoue, 2011; Terry et al., 2011). We have also recently identified another p114RhoGEF-mediated mechanism that drives apical cell constriction during neural tube morphogenesis in vertebrates via heterotrimeric G protein activation (Marivin et al., 2019). We found that DAPLE, an atypical, non-GPCR activator of heterotrimeric G proteins that is localized at apical cell junctions, (Aznar et al., 2015; Ishida-Takagishi et al., 2012; Landin Malt et al., 2020; Oshita et al., 2003), triggered Gβγ-dependent activation of p114RhoGEF to promote apical cell constriction in the neural tube of *Xenopus* (Marivin et al., 2019). Interestingly, a similar apical cell constriction mechanism involving Gβγ-dependent activation of p114RhoGEF was described soon after in *Drosophila*, although the upstream input was classic GPCR-mediated activation of G proteins (Garcia De Las Bayonas et al., 2019). Taken together, these observations suggest that heterotrimeric G protein signaling at apical cell junctions regulates the apical actomyosin network. Intriguingly, DAPLE has also been reported to bind directly to PAR3 (Ear et al., 2020), although the functional significance of this interaction is unknown. Prompted by these previous observations, we investigated the relationship between DAPLE, apical junctions, and the regulation of the apical actomyosin network in epithelial cells. Our results identify DAPLE as a component of junctional polarity complexes that maintains the apical cytoskeletal network to support the shape and function of homeostatic epithelial monolayers or multiciliated cells (MCCs) in the epidermis of *Xenopus* embryos. The underlying mechanism by which DAPLE instructs the apical actomyosin network from apical cell junctions involves two concomitant events at the molecular level—on one hand, DAPLE recruits CD2AP, a protein that stabilizes junctional and apical actin (Johnson et al., 2008; Kirsch et al., 1999; Tang and Brieher, 2013; Wang and Brieher, 2020), and on the other hand, it activates heterotrimeric G protein signaling leading to RhoA activation.

Results

DAPLE is required to maintain the shape and function of cell–cell junctions

To assess a possible role of DAPLE in the function of epithelial cell–cell junctions, we generated two DAPLE-depleted MDCK cell lines using nonoverlapping RNAi sequences (Fig. 1 A) and compared their ability to establish epithelial barrier function compared with control cells. For this, we used a well-established calcium switch protocol (Fig. 1 B). Briefly, we measured transepithelial electrical resistance (TEER) at different time points after replenishing the medium with Ca^{2+} to induce the formation of cell–cell junctions. Both DAPLE-depleted cell lines showed a marked reduction of the transient TEER peak observed at early time points (~4–8 h after Ca^{2+}), whereas no difference was observed when cell junctions had matured 24 h after Ca^{2+} replenishment (Fig. 1 B). The transient defect in TEER at early time points was not accompanied by an overt defect in the formation of cell–cell junctions, as assessed by the recruitment of the junctional markers ZO-1 and E-cadherin (Fig. S1 A). However, DAPLE-depleted cell monolayers at later time points or under steady-state culture conditions showed marked differences in cell–cell junction morphology compared with controls. More specifically, loss of DAPLE caused lateral and apical cell junctions to display higher deformability (Fig. 1, C and D). Deformation of lateral junctions was evidenced by quantification of the distribution of the lateral junction maker E-cadherin relative to the apical junction marker ZO-1 when the signals across the vertical axis of the monolayer were projected on the horizontal plane (Fig. 1 E). In control cells, ZO-1 and E-cadherin projections distributed as sharp peaks that aligned well with each other (Fig. 1 E). In contrast, E-cadherin intensity projections displayed a broader distribution than the sharp peak of ZO-1 in DAPLE-depleted cells (Fig. 1 E). Higher deformation was also observed across apical junctions, marked by ZO-1, on the horizontal plane of DAPLE-depleted cell monolayers (Fig. 1, C and D). This was quantitatively confirmed by the observation that DAPLE-depleted cells displayed diminished linearity (Fig. 1 F), which was also accompanied by a modest increase in apical cell area (Fig. 1 G). Similar changes in junctional linearity and apical area were observed upon depletion of DAPLE in another epithelial cell line (Eph4; Fig. S1, B–E). These morphological alterations were not accompanied by changes in the cellular abundance of junctional proteins or by mislocalization of epithelial polarity markers (Fig. S1, F–H), suggesting that they were not due to overt disruption of cell junctions or apicobasal polarity.

Taken together, these observations indicate that DAPLE is required to support the mechanical properties of epithelial cells that maintain cell–cell junction rigidity. Because these mechanical properties are required to resist tension and maintain epithelial integrity, we probed the effect of DAPLE depletion on epithelial barrier function upon chemically induced tensile stress. More specifically, Calyculin A (CalA) is known to induce

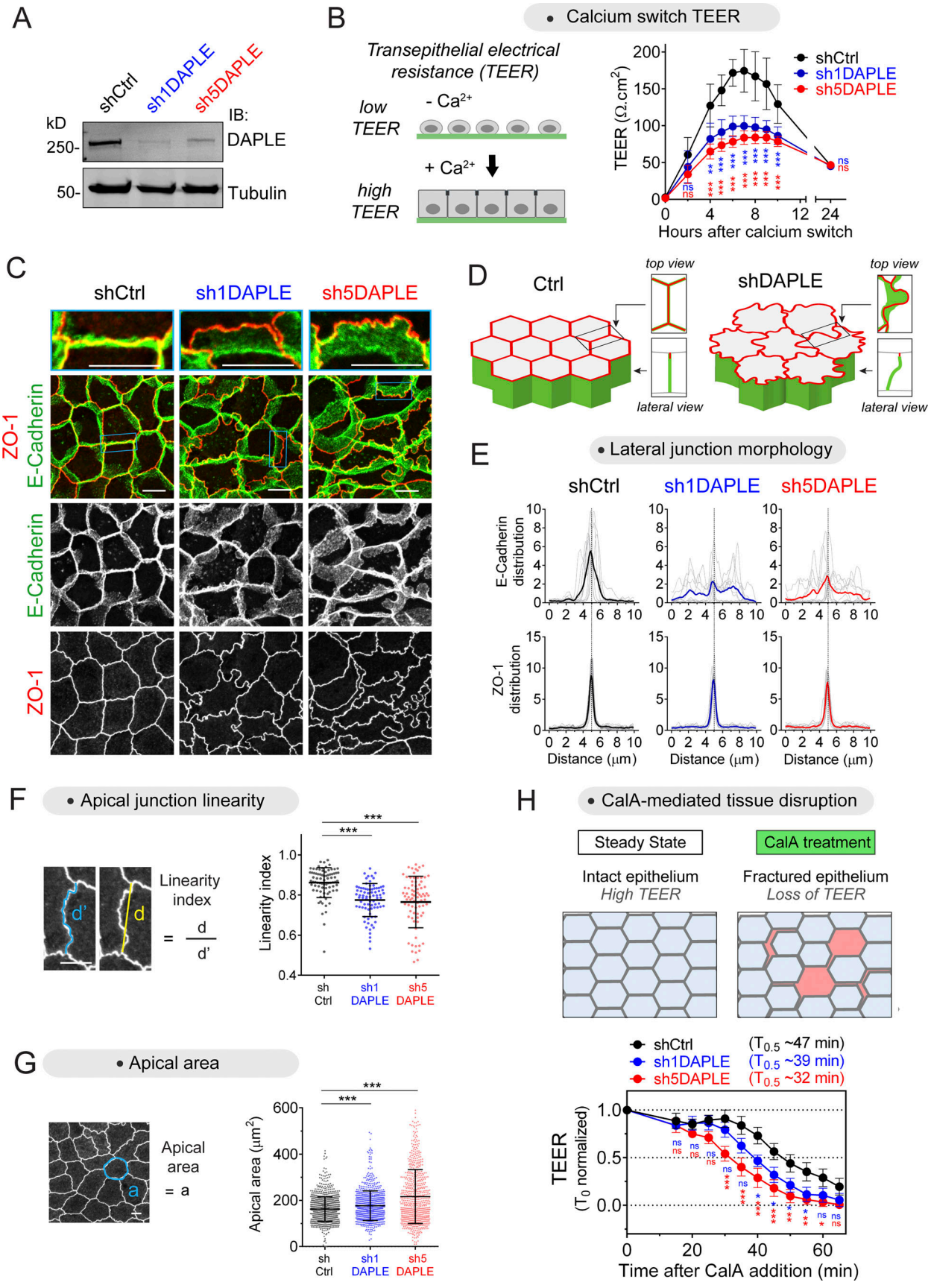

Figure 1. **Loss of DAPLE impairs epithelial barrier function establishment and alters cell–cell junction morphology. (A)** Validation of shRNA-mediated depletion of DAPLE in MDCK cells. Cells stably expressing shCtrl (control), sh1DAPLE, or sh5DAPLE RNAi sequences were generated by lentiviral transduction

and lysed for immunoblotting (IB) with the indicated antibodies. **(B)** Loss of DAPLE impairs the acquisition of epithelial barrier function upon calcium switch–induced cell–cell junction assembly. TEER of the indicated MDCK cell monolayers (shCtrl, sh1DAPLE, or sh5DAPLE) grown on Transwell filters was determined at the indicated times after Ca^{2+} switch. Mean ± SEM, n = 4 independent biological replicates; **, P < 0.01; ***, P < 0.001 compared with shCtrl using ANOVA test with Dunnett's multiple comparison correction. **(C and D)** Loss of DAPLE alters the morphology of cell–cell junctions. Established cell monolayers of the indicated MDCK cell lines (shCtrl, sh1DAPLE, or sh5DAPLE) were stained for E-cadherin and ZO-1 and imaged by confocal fluorescence microscopy. Representative images of maximum-intensity projections (top view) from three or more independent experiments are shown in C, and a 3D diagram of the observed phenotype is shown in D. **(E)** Distribution of E-cadherin and ZO-1 signals projected across 10 µm on the horizontal plane and centered at the cell–cell junction. Thick lines are the mean, and thin lines are the individual measurements of 10 cell–cell boundaries from one representative experiment. **(F and G)** Loss of DAPLE decreases the linearity of apical cell–cell junctions and increases apical cell area. Apical cell–cell junction linearity (F) or apical areas (G) were quantified from wide-field fluorescence microscopy images of ZO-1–stained cells. Scatter plot values are from 80 cell–cell junctions (2 experiments) in (F) or cells from 12 fields (3 experiments) in G. Mean ± SD; ***, P < 0.001, Mann–Whitney U test. **(H)** Loss of DAPLE impairs epithelial barrier function upon tensile stress. TEER of the indicated MDCK cell monolayers (shCtrl, sh1DAPLE, or sh5DAPLE) grown on Transwell filters was determined at the indicated times after CalA (80 nM) treatment. Mean ± SEM, n = 6 independent biological replicates; *, P < 0.05; **, P < 0.01; ***, P < 0.001 compared with shCtrl using ANOVA test with Dunnett's multiple comparison correction. All scale bars are 5 µm. Source data are available for this figure: SourceData F1.

increased tension at cell–cell junctions, which eventually leads to monolayer disruption and the subsequent loss of barrier function (i.e., loss of TEER; Acharya et al., 2018; Fig. 1 H). We found that loss of TEER upon CalA treatment occurred at earlier time points in DAPLE-depleted cells compared with controls, suggesting that loss of DAPLE makes cell monolayers less resilient to tensile stress (Fig. 1 H). In summary, these observations indicate that DAPLE is required to maintain the shape and function of cell–cell junctions in epithelial cells.

DAPLE controls cell junction morphology by associating with apical junctions via its PDZ-binding motif (PBM)

It has been previously reported that DAPLE localizes to apical junctions in epithelial cells, and that this localization is mediated by its C-terminal PBM (Ear et al., 2020; Marivin et al., 2019). Given this finding, we investigated if this subcellular targeting mechanism is required for DAPLE to determine cell junction morphology. To assess this, we stably expressed DAPLE WT or a PBM-deleted (ΔPBM) DAPLE mutant in the cellular background of DAPLE-depleted MDCK cells (Fig. 2 A). Cells expressing DAPLE WT displayed increased apical junction linearity and reduced apical area compared with DAPLE-depleted control cells (Fig. 2, B and C). DAPLE WT could be clearly detected at apical cell junctions (Fig. 2 B), in addition to being distributed across subapical cytoplasmic puncta, which might correspond to a previously reported pool of DAPLE that localizes to recycling endosomes (Aznar et al., 2017). In contrast, DAPLE ΔPBM was absent from apical cell junctions and failed to rescue the junction linearity and apical area phenotypes of DAPLE-depleted cells (Fig. 2, B and C). These results suggest that PBM-mediated targeting of DAPLE to apical cell junctions is required for maintaining proper cell junction morphology.

DAPLE associates with the PAR polarity complex via PAR3

Next, we set out to elucidate the mechanism by which DAPLE is targeted to apical cell junctions. DAPLE is known to use its PBM to directly bind to two bona fide junctional proteins, MPDZ and PAR3 (Ear et al., 2020; Marivin and Garcia-Marcos, 2019). Because MPDZ has been shown to be dispensable for the localization of DAPLE at apical junctions (Marivin and Garcia-Marcos, 2019), we focused our attention on PAR3. We found that DAPLE and PAR3 colocalized prominently at apical cell junctions in MDCK cells (Fig. 2 D). Because the pool of PAR3 associated with apical junctions is believed to exist in a complex with PAR6 and aPKC, known as the PAR polarity complex (PAR3–PAR6–aPKC; Chen and Macara, 2005; Morais-de-Sa et al., 2010; Nagai-Tamai et al., 2002; Rodriguez-Boulan and Macara, 2014; Suzuki et al., 2001), we investigated if DAPLE could associate with this complex. Coimmunoprecipitation experiments indicated that this is the case (Fig. 2 E). We found that PAR6 and PKCζ associated with DAPLE only in the presence of PAR3, whereas PAR3 associated with DAPLE regardless of the presence or absence of other components of the PAR complex (Fig. 2 E). These results indicate that DAPLE can associate with the PAR polarity complex via PAR3.

An intact PAR polarity complex is required for the recruitment of DAPLE to apical junctions

We began investigating if PAR3, the central scaffold of the PAR polarity complex, was required for DAPLE localization at apical junctions. For this, we attempted to generate an MDCK line stably depleted of PAR3 by using lentiviral RNAi (Fig. S2 A). After selection of transduced cells, we found that only some cells of the entire multiclonal pool were devoid of PAR3, which manifested as islands of PAR3-negative cells in mature MDCK monolayers (Fig. S2 A). Loss of PAR3 was accompanied by loss of ZO-1 (Fig. S2 A), indicating that, consistent with previous observations by others (Chen and Macara, 2005; Horikoshi et al., 2009; Sfakianos et al., 2007), loss of PAR3 causes overt defects in apical junction assembly and epithelial apicobasal polarity. Thus, even though DAPLE was also lost from junctions in PAR3-depleted cells (Fig. S2 B), this could be an indirect consequence of the overt disruption of apical junctions. This prompted us to seek alternative approaches to investigate the potential role of PAR3 on recruiting DAPLE to apical cell junctions. First, we found that when PAR3 was depleted acutely instead of chronically, as required for the experiments above with stable cell lines, DAPLE was lost from apical junctions but without the concomitant loss of ZO-1 (Fig. 2 F). Second, acute expression of a dominant-negative PAR3 construct that disrupts the PAR complex, corresponding to its N-terminal CR1 domain (PAR3N; Mizuno et al., 2003), also resulted in the loss of DAPLE from apical cell junctions without a concomitant loss of ZO-1 (Fig. 2 G). In contrast, DAPLE depletion did not affect the subcellular localization or abundance of PAR3 (Fig. S1, F and G), suggesting that PAR3 is an upstream regulator of DAPLE at

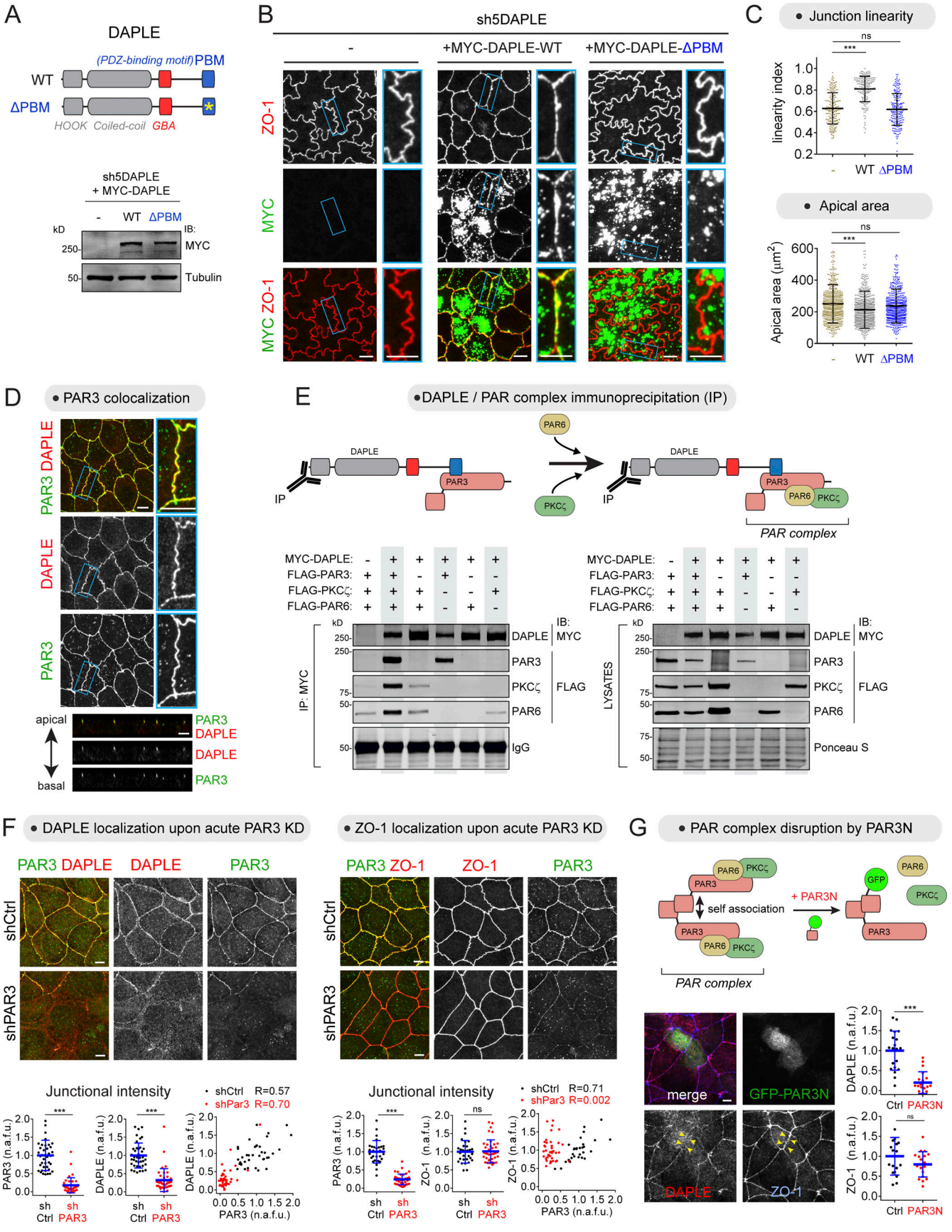

Figure 2. **Apical junction localization of DAPLE via PAR3 is required for maintaining proper cell–cell junction morphology. (A–C)** DAPLE requires its PBM to maintain proper cell–cell junction morphology. MYC-DAPLE WT or ΔPBM were stably expressed in DAPLE-depleted MDCK cells (sh5DAPLE) by

lentiviral transduction and cells lysed for IB with the indicated antibodies (A). Representative confocal fluorescence microscopy images of cells stained with ZO-1 and MYC are shown in B. Apical cell–cell junction linearity and cell apical areas were quantified from the ZO-1–stained images. Scatter plot values of 180 cell–cell junctions (linearity index) or of cells from 12 fields (apical area; three experiments). Mean ± SD; ***, P < 0.001, Mann–Whitney *U* test. **(D)** DAPLE colocalizes with PAR3 at apical cell junctions. MDCK cells were costained for endogenous DAPLE (red) and endogenous PAR3 (green) and imaged by confocal fluorescence microscopy. Upper panels are maximum-intensity projections of cell monolayers viewed from the top, and lower panels are a perpendicular optical cross-section of the monolayer. A magnified view of a cell–cell junction (blue rectangle) is shown on the right. **(E)** DAPLE associates with the PAR3–PAR6–aPKC (PAR) polarity complex via PAR3. Lysates of HEK293T cells expressing the indicated constructs were incubated with MYC antibodies, and immunoprecipitated (IP) proteins were detected by IB. The panel on the right corresponds to aliquots of the lysates used as starting material. One representative result of four experiments is shown. **(F)** Acute loss of PAR3 impairs the localization of DAPLE, but not of ZO-1, at apical cell junctions. MDCK cells were transduced with lentiviral particles for the expression of shCtrl (control) or shPAR3, costained for PAR3 and DAPLE or ZO-1, and analyzed by confocal fluorescence microscopy. Representative pictures of maximum-intensity projections are shown on the top, and quantification graphs of junctional intensities for DAPLE, PAR3 or ZO-1 are shown on the bottom of each panel (scatter plots with mean ± SD for 30–40 cell–cell boundaries from two independent experiments; ***, P < 0.001, Mann–Whitney *U* test). **(G)** Acute expression of dominant-negative PAR3N impairs the localization of DAPLE, but not ZO-1, at apical cell junctions. The diagram on the top depicts the dominant-negative action of PAR3N on PAR3 self-association that results in the disruption of the PAR3–PAR6–aPKC complex. MDCK cells were transfected with GFP-PAR3N; costained for GFP, DAPLE, and ZO-1; and analyzed by wide-field fluorescence microscopy. Representative fluorescence microscopy pictures are shown on the bottom left, and quantification of fluorescence intensities of DAPLE or ZO-1 at junctions between cells expressing GFP-PAR3N or at junctions between adjacent control cells are shown on the bottom right (scatter plots with mean ± SD for ∼20 cell–cell boundaries from three independent experiments; ***, P < 0.001, Mann–Whitney *U* test). Scale bar = 5 µm. Source data are available for this figure: SourceData F2.

apical junctions and not the other way around. Taken together with previous results, these observations indicate that DAPLE is recruited to the PAR polarity complex at apical cell junctions via PAR3 binding.

DAPLE is required to maintain the apical actomyosin network

We set out to investigate the mechanisms by which DAPLE, upon localization to apical junctions, supports the mechanical properties of epithelial cells that ensure proper cell morphology. We found that DAPLE depletion in MDCK cells led to a loss of F-actin across the entire apical domain, including junctional F-actin, without affecting the levels of F-actin at the basal domain (Fig. 3, A and B). This was also accompanied by a loss of nonmuscle myosin IIB (NMIIB) from the apical domain and junctions (Fig. 3 C), suggesting that DAPLE supports the assembly of the apical actomyosin network that is interconnected with apical junctions. Similar decreases in junctional F-actin and myosin were observed upon loss of DAPLE in Eph4 cells (Fig. S1, I–K). Next, we investigated the impact of DAPLE on the regulation of events upstream and downstream of apical actomyosin in epithelial cells. It has been previously shown that a junctional pool of RhoA is required to generate actomyosin-based forces at apical junctions (Priya et al., 2015). Consistent with the loss of apical actomyosin, we found that this regulatory pool of RhoA at cell junctions was diminished in DAPLE-depleted cells compared with controls (Fig. 3 D). We confirmed diminished junctional RhoA activity in DAPLE-depleted cells by using a reporter of GTP-bound, active RhoA (i.e., GFP-fused to anillin homology and pleckstrin homology [AHPH] domains; Fig. S3 A; Piekny and Glotzer, 2008; Priya et al., 2015). As for downstream events, we monitored the nucleocytoplasmic shuttling of the transcriptional regulators TAZ and YAP because it has been previously reported that this event is sensitive to upstream mechanical cues. More specifically, loss of tension in the circumferential actin belt that underlies apical junctions in epithelial cells causes the translocation of TAZ/YAP from the cytosol to the nucleus (Furukawa et al., 2017). We found that, whereas TAZ/YAP were excluded from the nucleus and localized predominantly in the cytosol of control cells, they accumulated in the nucleus of DAPLE-depleted cells (Fig. S3 B). Overall, these results indicate that DAPLE enables a mechanism that promotes the assembly of the apical actomyosin network that functions as a mechanical scaffold to maintain epithelial cell shape.

DAPLE mediates apical actomyosin activation upon tensile stress induction

To further characterize the impact of DAPLE on the regulation of the apical actomyosin network, we used CalA treatment as an experimental paradigm to induce acute activation of myosin II and subsequent tensile stress at cell junctions (Figs. 3 E and S4 A). First, we validated the mechanism of action of CalA in MDCK cells (Fig. S4, A–C). Previous reports in other cell types have proposed that CalA promotes myosin II–mediated forces by blocking myosin phosphatases, which leads to increased phosphorylation of the myosin regulatory light chain 2 (MLC2; Acharya et al., 2018; Chartier et al., 1991; Peterson et al., 2004). This results in increased myosin II–mediated contractility, and the subsequent tension at cell junctions creates a positive feedback mechanism that further reinforces myosin II recruitment and activation (Acharya et al., 2018). Consistent with this proposed mechanism of action, we found that CalA induced the accumulation of diphosphorylated (PP)-MLC2 (pT18/S19) at apical cell junctions, which was accompanied by an increase of junctional NMIIB (Fig. S4, B and C). Moreover, we found that inhibition of ROCK, an upstream input for myosin II phosphorylation, using Y27632, or the inhibition of myosin II contractile function using blebbistatin, greatly reduced CalA-induced accumulation of PP-MLC2 or NMIIB at apical cell junctions (Fig. S4, A–C). These results validate that CalA induces the acute activation of myosin II at apical cell junctions of MDCK cells through a mechanism that involves myosin phosphorylation and its contractile function.

Having established this system, we investigated the consequences of DAPLE loss on CalA-induced actomyosin activation. We found that DAPLE depletion prevented the accumulation of PP-MLC2 (Figs. 3 F and S4 D) and NMIIB (Figs. 3 G and S4 F) at apical cell junctions. This effect was not due to a global defect of myosin II activation in DAPLE-depleted cells

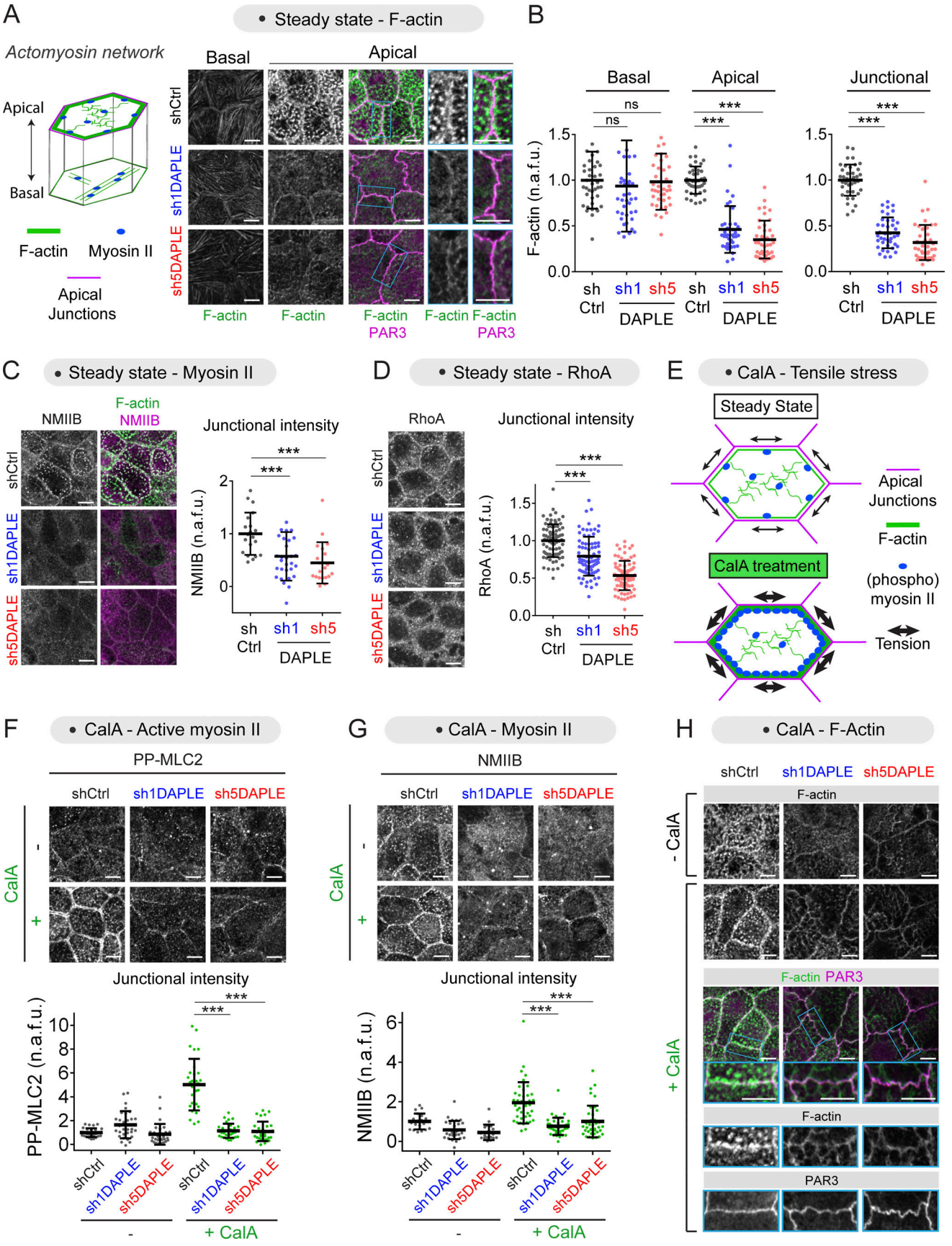

Figure 3. **Loss of DAPLE causes defects in the assembly of the apical actomyosin network. (A and B)** Loss of DAPLE decreases the level of apical but not basal F-actin. Established cell monolayers of the indicated MDCK cell lines (shCtrl, sh1DAPLE, or sh5DAPLE) were co-stained for F-actin and PAR3 and analyzed

by confocal fluorescence microscopy. Representative single optical sections at basal or apical levels are shown in A, with magnified views of selected cell–cell boundaries (blue rectangle) on the right. Quantification graphs of F-actin intensity at either basal or apical levels or at apical cell–cell junctions are shown in B (scatter plots with mean ± SD for ∼40 cells or cell–cell boundaries from three independent experiments; ***, P < 0.001, Mann–Whitney *U* test). **(C and D)** Loss of DAPLE decreases the level of NMIIB (C) or RhoA (D) at cell–cell junctions. Cells were processed and analyzed as in A and B but stained as indicated. Quantifications are displayed as scatter plots with mean ± SD for either ∼40 cell–cell boundaries from two independent experiments in C or ∼80 cell–cell boundaries from four independent experiments in D; ***, P < 0.001, Mann–Whitney *U* test). **(E)** Diagram depicting CalA-induced apical accumulation of active myosin II that depends on ROCK and myosin II activity (Fig. S4). **(F and G)** Loss of DAPLE prevents the accumulation PP-MLC2 (F) and NMIIB (G) at cell–cell junctions upon CalA treatment. MDCK cell lines were treated with CalA (80 nM, 20 min) as indicated, stained for PP-MLC2 or NMIIB, and analyzed by confocal fluorescence microscopy. Representative single optical sections at the level of apical junctions are shown on the top, and quantification graphs of junctional intensities for PP-MLC2 (F) or NMIIB (G) are shown on the bottom of each panel (scatter plots with mean ± SD for 30–40 cell–cell boundaries from at least two independent experiments; ***, P < 0.001 compared with shCtrl, Mann–Whitney *U* test). **(H)** Loss of DAPLE distorts junctional F-actin assemblies upon CalA treatment. MDCK cell lines were treated with CalA (80 nM, 20 min) as indicated, stained for F-actin and PAR3, and analyzed by confocal fluorescence microscopy. Representative single optical sections at the level of apical junctions from three independent experiments are shown. Magnified views of cell–cell junctions (blue rectangles) are depicted on the bottom. All scale bars are 5 µm.

because (a) the induction of PP-MLC2 levels upon CalA treatment at the basal domain of DAPLE-depleted cells was similar to that observed in control cells (Fig. S4 E), and (b) the total cellular levels of PP-MLC2 or NMIIB, as determined by immunoblotting, were not significantly different in DAPLE-depleted cells compared with control cells (Fig. S4 G). CalA treatment also enhanced F-actin at apical junctions in control but not DAPLE-depleted cells (Fig. 3 H). Instead, CalA-treated DAPLE-depleted cells displayed a reticular pattern of faint F-actin cables across the apical domain that connected to apical cell junctions. Taken together with previous results, these observations indicate that DAPLE contributes to the maintenance of the apical actomyosin network by ensuring two interrelated processes: one, the assembly of apical F-actin, and, two, the recruitment and activation of myosin II.

DAPLE is required for CD2AP junctional localization

As the next step, we set out to mechanistically link the junctional localization of DAPLE to its regulation of the apical actomyosin network and related morphological changes. In other words, how does DAPLE remodel apical actomyosin once it has been recruited to apical junctions? While previous evidence suggests that DAPLE might promote myosin II–dependent contractility by activating heterotrimeric G proteins in the context of neural tube morphogenesis (Marivin et al., 2019), the mechanism by which it might favor the assembly of apical F-actin was less clear. We noticed that the phenotype of diminished F-actin at the apical domain and junctions upon loss of DAPLE resembled that recently described upon loss of CD2AP, a protein that localizes to apical cell junctions in MDCK cells to stabilize actin (Tang and Brieher, 2013; Wang and Brieher, 2020). Prompted by this similarity, we investigated if DAPLE was required for the junctional localization of CD2AP. While immunoblotting revealed that DAPLE depletion did not change total levels of CD2AP, immunofluorescence staining showed a pronounced reduction of CD2AP at apical cell junctions (Fig. 4 A). These results suggested that DAPLE mediates the recruitment of CD2AP to apical junctions.

DAPLE and CD2AP coexist at actin-nucleating foci of apical junctions

DAPLE and CD2AP partially colocalized at apical cell junctions of MDCK cells (Fig. 4 B, left). Within apical junctions, CD2AP has been previously shown to localize at sites of actin nucleation (Tang and Brieher, 2013), which are characterized by containing a pool of F-actin insensitive to depolymerization induced by Latrunculin B. We found not only that both CD2AP and DAPLE accumulate at Latrunculin B–resistant foci at apical junctions, but also that their colocalization became much more prominent under these conditions than in untreated cells (Fig. 4 B, right).

DAPLE binds directly to CD2AP via an SH3-binding motif

Based on the requirement of DAPLE for CD2AP localization at cell junctions and the prominent colocalization of the two proteins, we hypothesized that DAPLE and CD2AP might bind directly to each other. A purified GST-fused C-terminal fragment of DAPLE (DAPLE-CT; Fig. 5 A) pulled down full-length CD2AP from HEK293T cell lysates (Fig. 5 B), and a purified GST-fused fragment of CD2AP corresponding to its second SH3 domain (SH3-2; Fig. 5 A) bound robustly full-length DAPLE from HEK293T cell lysates (Fig. 5 C). We confirmed that DAPLE-CT binds directly to CD2AP SH3-2 by using purified proteins (Fig. 5 D). In contrast, the SH3-1 and SH3-3 domains of CD2AP bound DAPLE very weakly (Fig. 5 C), and no binding was detected with 13 other SH3 domains from different proteins (Fig. 5 E), indicating that the interaction of DAPLE occurs specifically with the SH3-2 domain of CD2AP. Furthermore, a shorter C-terminal fragment of DAPLE (DAPLE-CT2, aa 1,746–2,028) was sufficient to bind CD2AP (Fig. 5 F), and this fragment contained a putative SH3-binding motif (SH3-BM) with similarity to previously reported CD2AP binding sequences containing a PXXXPR consensus (Moncalian et al., 2006; Rouka et al., 2015; Fig. 5 G). Replacement of the two most conserved positions of this consensus motif (P1941 and R1946) by alanines (P1941A/R1946A = SH3-BM* mutant) resulted in reduced binding of full-length CD2AP to DAPLE-CT (Fig. 5 H) or binding of full-length DAPLE to CD2AP SH3-2 (Fig. 5 I). These results demonstrate that DAPLE interacts directly with CD2AP through an SH3-binding motif located in its C-terminal region.

DAPLE requires its Gα-binding-and-activating (GAB) motif and its SH3-BM to maintain normal junctional morphology

Having established that DAPLE binds to CD2AP, an actin-stabilizing factor, and knowing that DAPLE also activates heterotrimeric G proteins, a signaling mechanism previously shown to induce myosin-dependent apical cell constriction

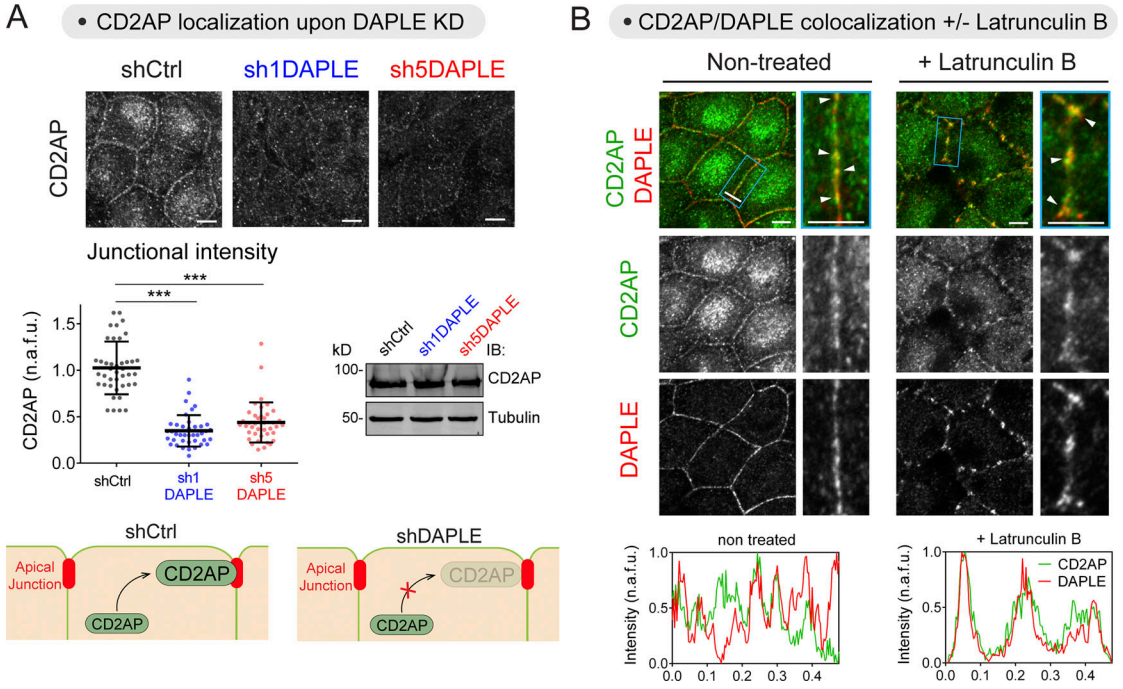

Figure 4. **DAPLE is required for CD2AP recruitment to cell–cell junctions. (A)** Loss of DAPLE impairs the localization of CD2AP at cell–cell junctions. Monolayers of the indicated MDCK cell lines were stained for CD2AP and analyzed by confocal fluorescence microscopy. Representative pictures of maximum-intensity projection of the apical domain (1 µm) are shown on the top, a quantification graph of junctional intensities for CD2AP is shown on the bottom left (scatter plots with mean ± SD for ∼40 cell–cell boundaries from three independent experiments; ***, P < 0.001, Mann–Whitney *U* test), and a representative immunoblot for total CD2AP expression is shown on the bottom right. **(B)** DAPLE colocalizes with CD2AP at apical cell–cell junctions and in Latrunculin B–resistant foci. Nontreated or Latrunculin B–treated (2 h, 10 µM) MDCK cells were stained for CD2AP and DAPLE and analyzed by confocal fluorescence microscopy. Upper panels are maximum-intensity projections of the apical domain (1 µm) of cell monolayers viewed from the top, and lower panels are fluorescent intensity profiles along cell junctions shown in the magnified areas (blue rectangles). White arrowheads indicate colocalization at cell–cell junctions. Source data are available for this figure: SourceData F4.

during neural tube morphogenesis (Marivin et al., 2019), we set out to further dissect the molecular mechanisms by which DAPLE maintains proper epithelial cell shape. For this, we assessed the ability of different DAPLE constructs to rescue morphological alterations associated with DAPLE depletion (Fig. 6 A). More specifically, we evaluated apical junction linearity and apical area when DAPLE WT, DAPLE GBA* (bearing an F1675A mutation that precludes G protein binding and activation; Aznar et al., 2015), DAPLE SH3-BM* (which precludes CD2AP binding), or DAPLE ΔPBM (which precludes PAR3 binding and DAPLE localization to apical cell junctions, Fig. 2) was stably expressed in the cellular background of DAPLE-depleted MDCK cells (Fig. 6, A and B). The premise for using these mutants is that each one specifically disrupts one functional interaction of DAPLE with G proteins, CD2AP, or PAR3, without affecting any of the other two interactions. We validated that this premise by using protein–protein binding assays (Fig. S5, A–D). We also validated that DAPLE WT and DAPLE GBA* rescued the junctional localization of CD2AP, whereas DAPLE SH3-BM* and DAPLE ΔPBM did not (Fig. S5, E and F). Failure to rescue CD2AP localization by DAPLE SH3-BM* is expected from its diminished binding to CD2AP (Fig. 5), whereas for DAPLE ΔPBM it is explained best by the lack of junctional localization of this mutant (Fig. 2). Consistent with the latter observation, we found that CD2AP associated with PAR3 in vitro only when DAPLE bridges both proteins to form a CD2AP–DAPLE–PAR3 ternary complex (Fig. S5 G), suggesting that CD2AP is recruited by the DAPLE–PAR3 complex at apical junctions. Using this collection of mutants, we found that both DAPLE GBA* and DAPLE SH3-BM* failed to recapitulate the restoration of junctional linearity observed with DAPLE WT (Fig. 6, C and D), therefore mimicking the observations in cells expressing DAPLE ΔPBM (Fig. 2). Similar trends were observed for the different mutants in terms of apical cell area, although they were somewhat less pronounced than the differences in junctional linearity (Fig. 6 D). Compared with DAPLE ΔPBM, which failed to localize to apical cell junctions (Fig. 2), both DAPLE GBA* and DAPLE SH3-BM* localized to apical cell junctions similarly to DAPLE WT (Fig. 6, C and D). These results suggest a mechanism by which targeting of DAPLE to apical cell junctions is necessary but not sufficient to regulate epithelial cell shape. Once at apical cell junctions, DAPLE also requires the triggering of two additional independent events: recruitment of CD2AP via its SH3-BM and activation of G proteins via its GBA motif.

The GBA motif and the SH3-BM of DAPLE have different roles in the regulation of apical actomyosin

We followed up by characterizing the impact of DAPLE mutants on apical actomyosin regulation (Fig. 7 A). First, we found that expression of DAPLE WT in MDCK cells depleted of endogenous

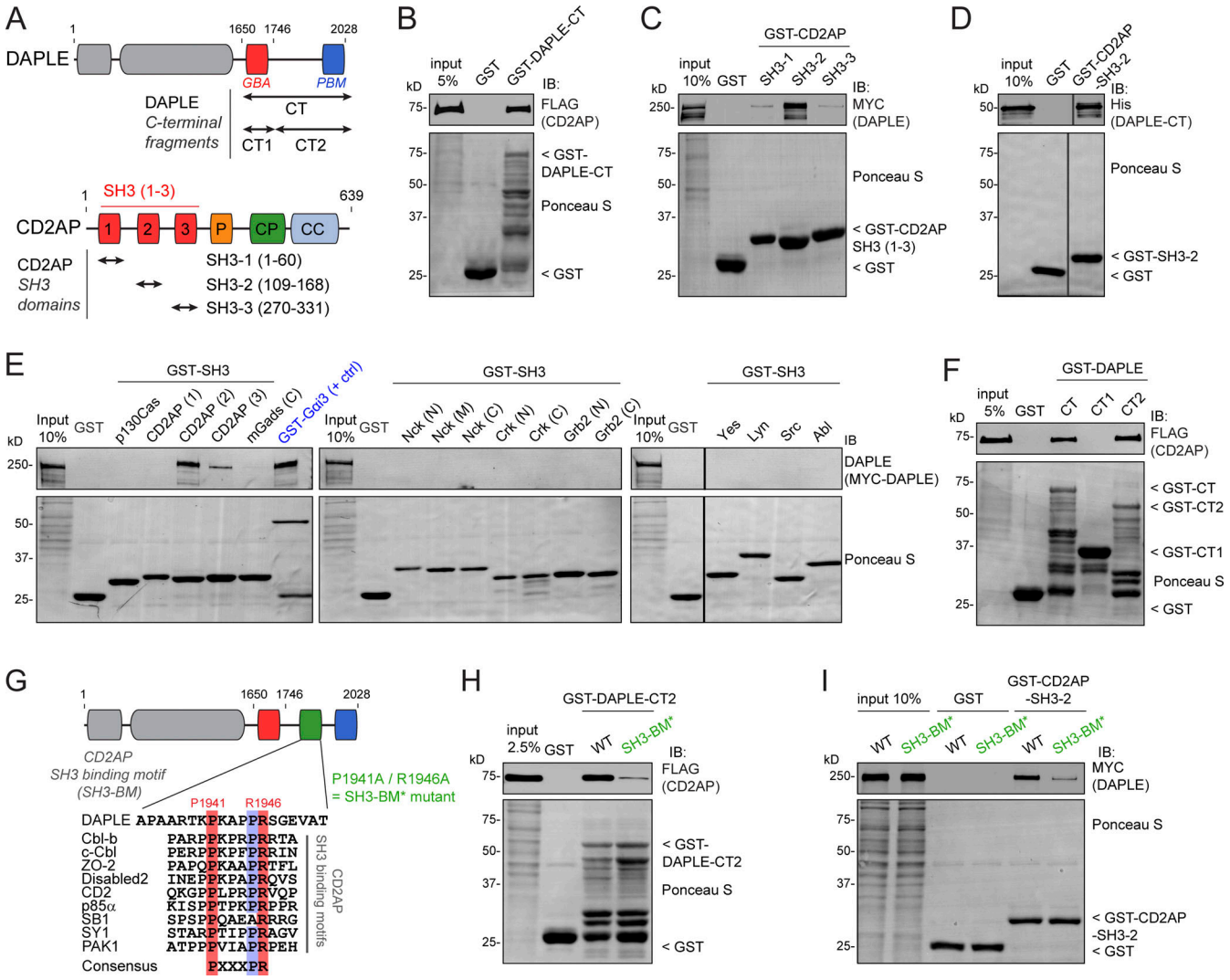

Figure 5. **DAPLE directly binds CD2AP through an SH3-binding motif. (A)** Bar diagram depicting DAPLE (top) and CD2AP (bottom) domains and indicating the fragments of each one used for experiments presented in this figure. CC, coiled coil; CP, capping protein binding; GBA, Gα-binding-and-activating motif; P, proline-rich; SH3, Src homology 3 domain. **(B)** Full-length CD2AP binds to the C-terminal (CT) region of DAPLE. Lysates of HEK293T transfected with FLAG-CD2AP were incubated with GST or GST-DAPLE-CT immobilized on glutathione-agarose beads. Bead-bound proteins were detected by Ponceau S staining or by IB. **(C)** Full-length DAPLE binds to the SH3-2 domain of CD2AP. Lysates of HEK293T transfected with MYC-DAPLE were incubated with GST or GST-CD2AP SH3-1, SH3-2, or SH3-3 immobilized on glutathione-agarose beads. Bead-bound proteins were detected by Ponceau S staining or IB. **(D)** CD2AP binds directly to DAPLE. Purified His-DAPLE-CT was incubated with purified GST-CD2AP SH3-2 or GST immobilized on glutathione-agarose beads. Bead-bound proteins were detected by Ponceau S staining or IB. The vertical lines indicate that the images were assembled by splicing lanes from the same experiment and membrane. **(E)** DAPLE binds to SH3-2 domain of CD2AP but not to many other SH3 domains. Lysates of HEK293T cells transfected with MYC-DAPLE were incubated with GST, GST-Gαi3 (as positive control), and the indicated GST-fused SH3 domains immobilized on glutathione-agarose beads. Bead-bound proteins were detected by Ponceau S staining or IB. One representative result of three independent experiments. The vertical lines indicate that the images were assembled by splicing lanes from the same experiment and membrane. **(F)** DAPLE CT2 (1,746–2,028) fragment is sufficient to bind CD2AP. Lysates of HEK293T transfected with FLAG-CD2AP were incubated with GST or GST-DAPLE C-terminal fragments immobilized on glutathione-agarose beads. Bead-bound proteins were detected by Ponceau S staining or by IB. **(G)** Identification of a putative CD2AP SH3 binding motif in the C-terminal region of DAPLE. Alignment of DAPLE sequence with multiple CD2AP SH3 binding motifs from other proteins that contain the consensus PXXXPR sequence. **(H)** Mutation of DAPLE's SH3 binding motif decreases binding to CD2AP. Lysates of HEK293T transfected with FLAG-CD2AP were incubated with GST, GST-DAPLE-CT2 WT, or P1941A/R1946A (SH3-BM*) mutant immobilized on glutathione-agarose beads. Bead-bound proteins were detected by Ponceau S staining or IB. **(I)** Binding of full-length DAPLE to CD2AP is impaired upon mutation of the SH3 binding motif. Lysates of HEK293T transfected with MYC-DAPLE (WT or SH3-BM* mutant) were incubated with GST or GST-CD2AP SH3-2 immobilized on glutathione-agarose beads. Bead-bound proteins were detected by Ponceau S staining or IB. All results presented are representative of $n \geq 2$ experiments. All scale bars are 5 µm. Source data are available for this figure: SourceData F5.

DAPLE increased the levels of F-actin at apical junctions (Fig. 7, B and C). This could not be recapitulated in DAPLE-depleted cells expressing ectopic DAPLE GBA*, DAPLE SH3-BM*, or DAPLE ΔPBM (Fig. 7, B and C). Levels of junctional RhoA were also increased by DAPLE WT (Fig. 7, D and E). However, in contrast with the F-actin results, not all mutants behaved the same with regard to RhoA regulation. Although DAPLE GBA* and DAPLE ΔPBM failed to recapitulate the increase of junctional RhoA

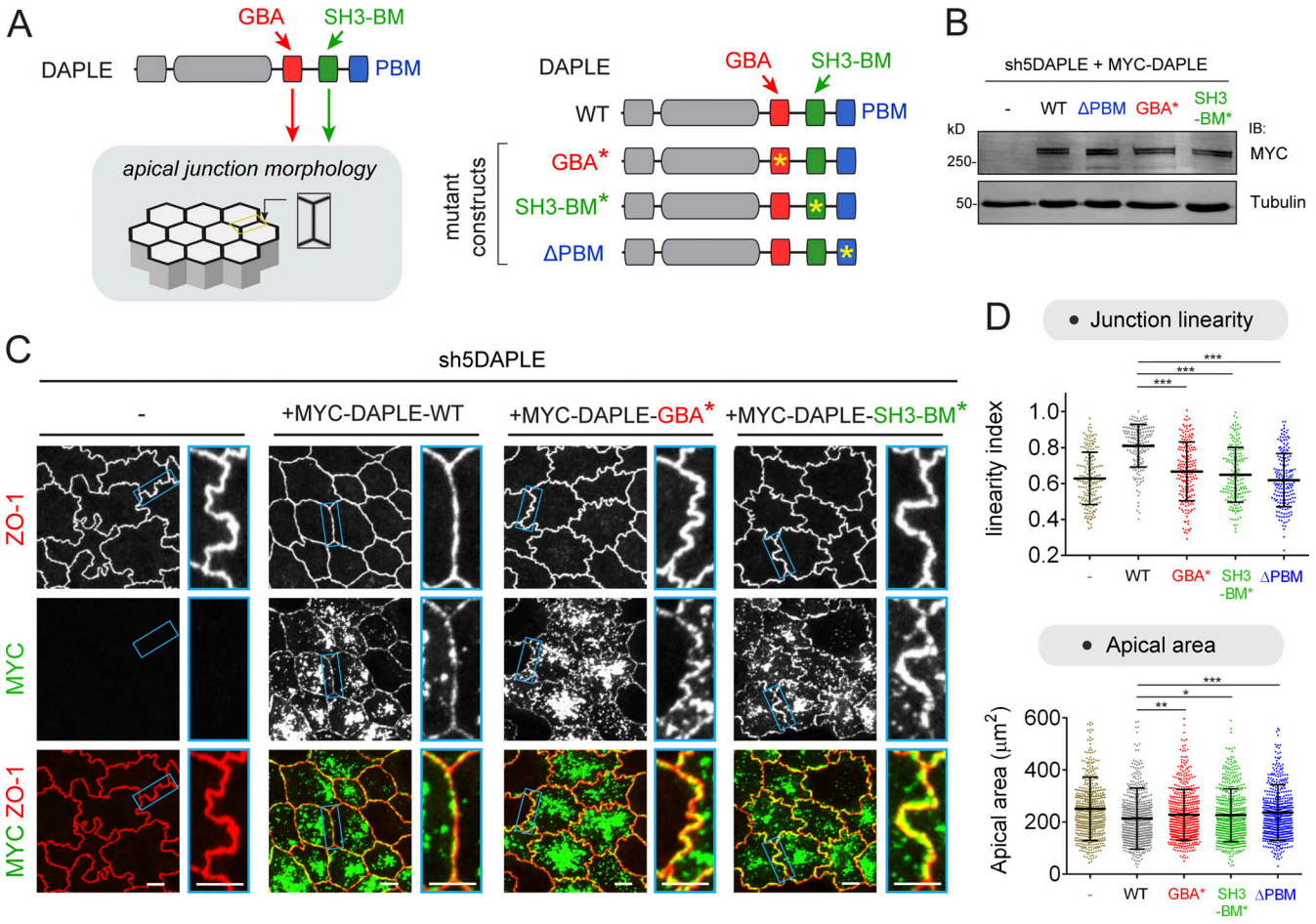

Figure 6. **DAPLE maintains proper cell–cell junction morphology via its SH3-binding motif (SH3-BM) and its Gα-binding and -activating (GBA) motif.** **(A)** Diagram depicting DAPLE's functional modules potentially involved in the regulation of junctional morphology and mutants used to investigate this function. **(B)** MYC-DAPLE WT, GBA*, SH3-BM*, or ΔPBM was stably expressed in DAPLE-depleted MDCK cells (sh5DAPLE) by lentiviral transduction, and cells were lysed for IB with the indicated antibodies. **(C and D)** DAPLE requires its GBA motif and its SH3-BM to maintain proper cell–cell junction morphology. Representative single optical sections at the level of apical junctions of the indicated MDCK cell lines stained for ZO-1 and MYC are shown in C. Apical cell–cell junction linearity and apical cell areas were quantified from the ZO-1 staining images. Scatter plot values are for 180 cell–cell junctions (linearity index) or for cells from 12 fields (apical area; three experiments). Mean ± SD; *, $P < 0.05$; **, $P < 0.01$; ***, $P < 0.001$, Mann–Whitney *U* test. Quantifications for cells not expressing MYC-DAPLE (–), MYC-DAPLE WT, and DAPLE ΔPBM mutant are same as in Fig. 3 C, and they are shown here again for direct comparison across all mutants. All scale bars are 5 µm. Source data are available for this figure: SourceData F6.

observed with DAPLE WT, the expression of DAPLE SH3-BM* had an effect similar to that of DAPLE WT (Fig. 7, D and E). Next, we investigated the recruitment of NMIIB but failed to observe changes upon DAPLE WT expression under steady-state culture conditions. This prompted us to investigate NMIIB upon CalA treatment. Under these conditions, we found increased levels of NMIIB at apical junctions in cells expressing DAPLE WT, whereas NMIIB levels remained low in DAPLE-depleted control cells (Fig. 7, F and G). Analogous to the observations with RhoA, we found that DAPLE SH3-BM* recapitulated the increase of junctional NMIIB upon CalA treatment observed with DAPLE WT, whereas DAPLE GBA* and DAPLE ΔPBM failed to do so (Fig. 7, F and G). Taken together, these results indicate that the GBA motif and the SH3-BM have different roles in the regulation of apical actomyosin by DAPLE. While both of them are required to support apical F-actin assemblies, only the GBA motif is required for RhoA and myosin II regulation.

Loss of DAPLE disrupts the apical actin network of epithelial cells in vivo

To further substantiate the biological significance of the DAPLE-mediated mechanism gleaned from cultured cells, we evaluated the impact of loss on DAPLE on the assembly of the apical actin cytoskeleton of epithelial cells in vivo. For this, we turned our attention to the MCCs of the epidermis of *Xenopus* embryos. These cells possess a prominent network of apical F-actin that is crucial for the function of their cilia in directing fluid flow across the cellular surface (Antoniades et al., 2014; Park et al., 2008; Werner et al., 2011), a feature conserved across MCCs in other organisms and tissues like mammalian ependymal or airway epithelia (Butler and Wallingford, 2017; Mahuzier et al., 2018; Tateishi et al., 2017). To be able to determine if *Xenopus* DAPLE (xDAPLE) is localized at the apical junctions of MCCs in the *Xenopus* skin, we generated and validated a new antibody. Briefly, this antibody recognized the purified antigen and full-

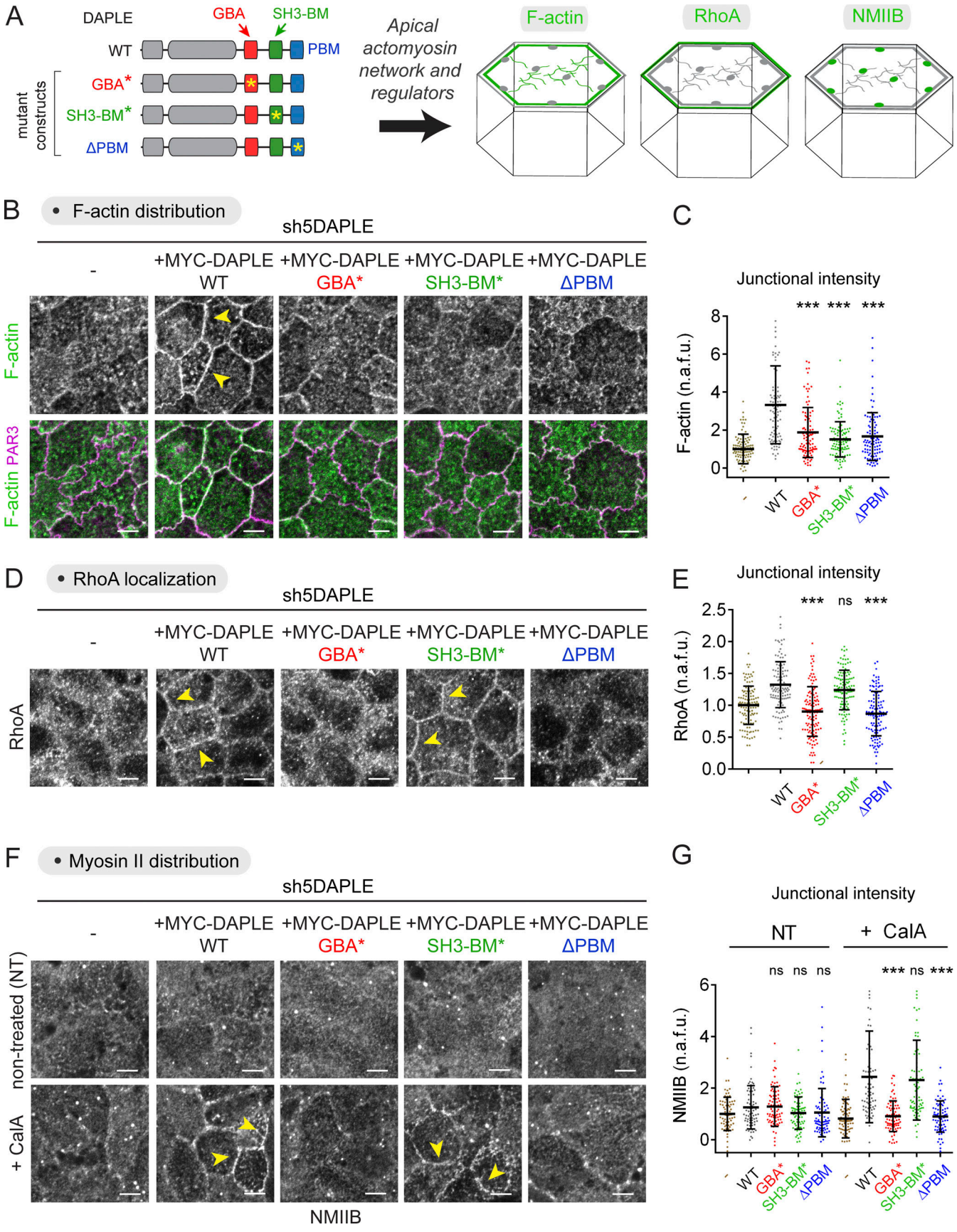

Figure 7. **DAPLE's GBA motif and SH3-BM motif have distinct regulatory activities on junctional actomyosin. (A)** Diagram depicting DAPLE's functional modules involved in the regulation of junctional actomyosin and mutants used to investigate this function. **(B and C)** DAPLE WT, but not GBA*, SH3-BM*, or

ΔPBM mutants, rescues the loss of junctional F-actin observed in DAPLE-depleted cells. MYC-DAPLE WT, GBA*, SH3-BM*, or ΔPBM were stably expressed in MDCK sh5DAPLE cells by lentiviral transduction. Representative single optical sections at the level of apical junctions of the indicated MDCK cell lines stained for F-actin and PAR3 are shown in B, and the quantification of F-actin fluorescence intensity is shown in C. Scatter plot values are for ∼100 cell–cell boundaries (five experiments). Mean ± SD; ***, P < 0.001 compared with DAPLE WT using the Mann–Whitney *U* test. **(D and E)** DAPLE WT and SH3-BM* mutant, but not GBA* or ΔPBM mutants, rescue the loss of junctional RhoA observed in DAPLE-depleted cells. Representative pictures and quantification as in B and C. Scatter plot values are for ∼120 cell–cell boundaries (six experiments). Mean ± SD; ***, P < 0.001 compared with DAPLE WT using the Mann–Whitney *U* test. **(F and G)** DAPLE WT and SH3-BM* mutant, but not GBA* or ΔPBM mutants, rescue the loss of junctional NMIIB after CalA treatment observed in DAPLE-depleted cells. Cells were processes and analyzed and in B and C, except that some cells were treated with CalA (80 nM, 20 min). Scatter plot values are for ∼80 cell–cell boundaries (four experiments). Mean ± SD; ***, P < 0.001 compared with DAPLE WT using the Mann–Whitney *U* test. All scale bars are 5 µm. Yellow arrowheads indicate examples of junctional signals for different markers.

length xDAPLE expressed in HEK293T cells by immunoblotting (Fig. 8 A). Also, immunostaining of the *Xenopus* epidermis with this antibody revealed a prominent signal specifically at the apical junctions of MCCs (identified by the presence of acetylated tubulin in cilia, Fig. 8 B), which was lost upon injection of a previously validated (Kobayashi et al., 2005; Marivin et al., 2019) morpholino (MO) against xDAPLE (Fig. 8 C). xDAPLE was asymmetrically distributed across the horizontal plane of the tissue, an observation consistent with previous findings in MCCs of other tissues that manifest planar cell polarization, such as the ependyma or the trachea (Nakayama et al., 2021; Takagishi et al., 2020; Takagishi et al., 2017). Loss of xDAPLE led to a marked decrease of F-actin at the apical and subapical level (Fig. 8, D–F), two interconnected pools of F-actin that are associated, respectively, with the basal bodies and rootlets of cilia (Werner et al., 2011). Consistent with this loss of cilia-associated F-actin, we also observed defects in the length, number, and organization of cilia based on the signal from the membrane-anchored lineage tracer (Fig. 8 D), which was confirmed by acetylated tubulin staining (not depicted). These results demonstrate that DAPLE is a junctional protein required for the assembly of the apical actin network of epithelial cells in vivo.

Discussion

How cells adopt and maintain their shape is a central question of cell biology. This is particularly relevant for epithelial cells, which serve as the building blocks used to maintain or remodel many tissues and organs. The main advance provided by our work is the identification of a molecular mechanism linking junctional polarity complexes to the regulation of the apical actomyosin network of epithelial cells. This sheds light onto how the protein complexes that determine epithelial polarity instruct the effector machinery that shapes cells. Our results strongly support a model (Fig. 8 G) in which the protein DAPLE leverages its association with the PAR polarity complex as a positional cue to orchestrate the assembly of the apical actomyosin network from apical cell junctions. DAPLE uses three discrete motifs to achieve this: PBM, GBA, and SH3-BM. While PAR association is mediated via PBM binding to one of PAR3's PDZ domains (Ear et al., 2020), DAPLE uses two other discrete motifs to mediate the effector mechanisms that promote apical actomyosin assembly. The first one corresponds to a previously described motif that is used by DAPLE and other non-GPCR cytoplasmic proteins to activate heterotrimeric G protein signaling (Coleman et al., 2016; de Opakua et al., 2017; DiGiacomo et al., 2018; Garcia-Marcos et al., 2009), whereas the second one corresponds to a newly identified motif that recruits CD2AP to apical junctions. Both motifs must be functionally intact to support proper apical actomyosin assembly, suggesting that their functions must work simultaneously at cell junctions. Interestingly, while both G protein regulation and CD2AP recruitment are required to assemble the F-actin component of the apical actomyosin network, CD2AP appears to be dispensable for myosin II and RhoA recruitment (Fig. 7). It is tempting to speculate that the two arms of the DAPLE-mediated effector mechanism exert complementary functions in apical actomyosin regulation—CD2AP ensures the formation actin cables, whereas heterotrimeric G proteins lead to RhoA-dependent activation of myosin II. Although this is a tantalizing idea, the possibility that the heterotrimeric G protein–RhoA axis also contributes to F-actin stabilization through one of RhoA's targets (e.g., formins) cannot be ruled out.

Since the initial discovery of PAR proteins in *C. elegans*, the complex formed by PAR3, PAR6, and aPKC has been known to link cell polarity to regulation of the actin cytoskeleton (Nance and Zallen, 2011). In epithelial cells, this PAR polarity complex promotes the assembly of an apical actomyosin network that maintains cell shape and drives the generation of polarized contractile forces (Chen and Macara, 2005; David et al., 2010; Harris and Peifer, 2004; Nance and Zallen, 2011; Silver et al., 2019; Zallen and Wieschaus, 2004). While the PAR polarity complex occupies a privileged subcellular location, i.e., apical cell junctions, to coordinate tissue-level mechanics and cell architecture, the specific and direct molecular links that physically connect it to the apical actin cytoskeleton have remained ill defined. For example, aPKC-mediated phosphorylation of various regulators of the actin cytoskeleton has been shown to modulate epithelial cell architecture (Ishiuchi and Takeichi, 2011; Nakajima and Tanoue, 2011), but it is unclear whether these regulatory mechanisms operate specifically from the PAR polarity complex at apical cell junctions. In this regard, our work establishes DAPLE as an adaptor that "hard-wires" the PAR polarity complex to the apical cytoskeleton by recruiting the actin-binding protein CD2AP. Much as in our observations here with DAPLE, CD2AP has been shown to operate at apical cell junctions but to influence the assembly of an actin network throughout the apical domain (Tang and Brieher, 2013; Wang and Brieher, 2020).

The second component of the mechanism by which DAPLE propagates signals from junctional complexes to the apical cytoskeleton is through activation of heterotrimeric G proteins ($G\alpha\beta\gamma$). This finding fills a gap in an emerging area of investigation on the mechanisms by which apical actomyosin is

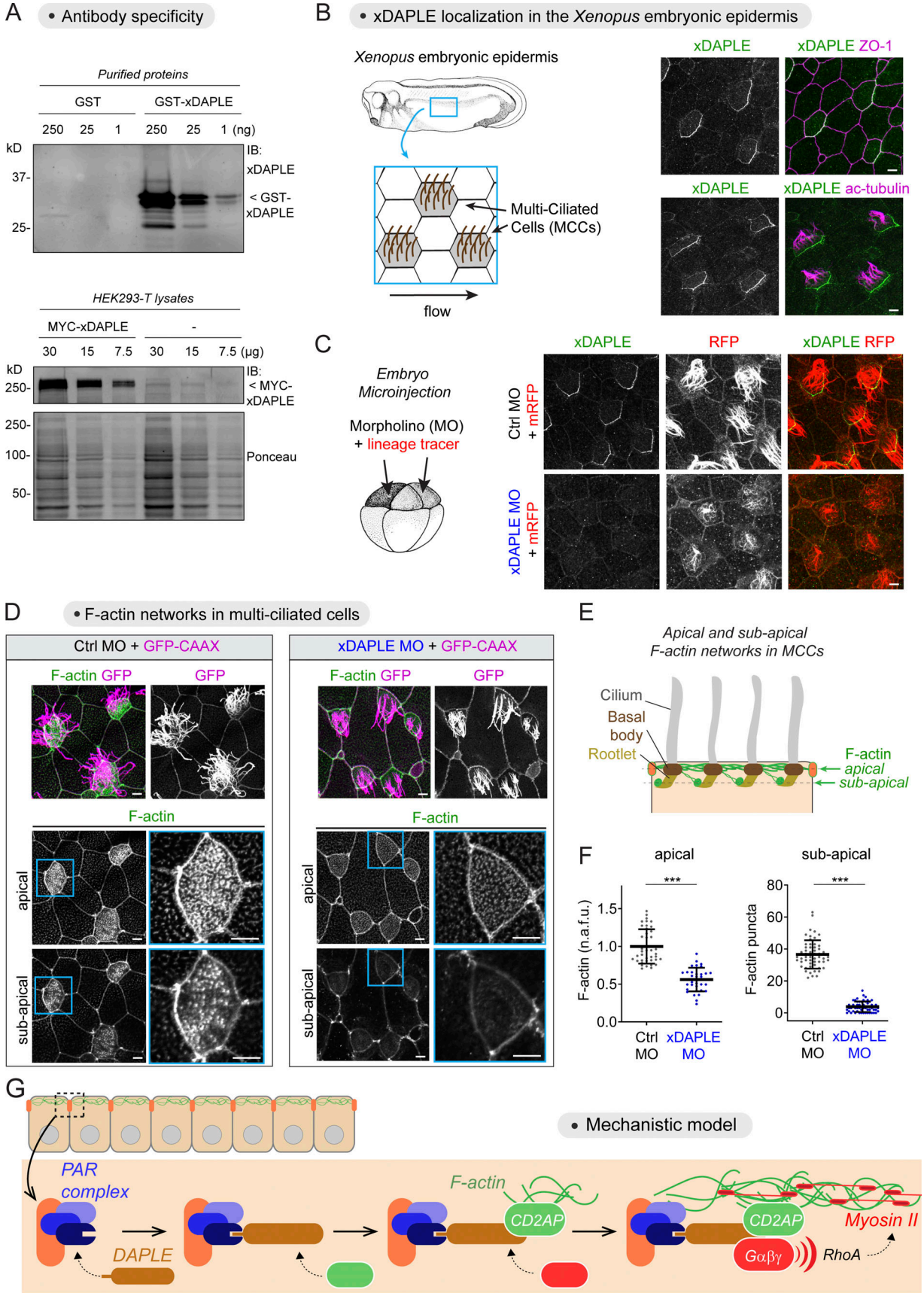

Figure 8. **Loss of DAPLE causes apical actin defects in MCCs of the *Xenopus* embryonic epidermis. (A)** IB detection of purified GST-xDAPLE (top) or MYC-xDAPLE in HEK293T lysates (bottom) using a rabbit polyclonal antibody raised against xDAPLE. **(B and C)** xDAPLE localizes at apical junctions of MCCs in the

Xenopus epidermis. Uninjected embryos (B) or embryos coinjected with MO (Ctrl or xDAPLE) and mRNA for a membrane-anchored RFP (mRFP) tracer (C) were immunostained at stage 28 and analyzed by confocal microscopy. Representative maximum-intensity projections of the apical domain (2 µm) of epidermal cells are shown (n = 3). **(D–F)** Depletion of xDAPLE decreases apical and subapical F-actin in MCCs of the *Xenopus* epidermis. Embryos coinjected with MO (Ctrl or xDAPLE) and mRNA for a membrane-anchored GFP (GFP-CAAX) tracer were immunostained at stage 28 for GFP and F-actin and analyzed by confocal microscopy. Representative images of apical and subapical F-actin (see scheme in E) are shown in D (maximum-intensity projections of 0.8-µm thickness at the level of apical F-actin or subapical F-actin), and quantifications of fluorescence intensities are shown in F. Scatter plot values are for 40–60 MCCs from four experiments. Mean ± SD; ***, P < 0.001 using the Mann–Whitney *U* test. **(G)** Proposed model for how DAPLE association with the PAR complex at apical junctions promotes apical actomyosin assembly by simultaneously recruiting the actin stabilizer CD2AP and activating Gαβγ-mediated RhoA signaling. All scale bars are 5 µm. Source data are available for this figure: SourceData F8.

regulated by heterotrimeric G proteins and cell junctions. The G protein–regulated RhoGEF named p114RhoGEF (Cysts or Dp114RhoGEF in *Drosophila*), which localizes at apical cell junctions (Nakajima and Tanoue, 2011; Terry et al., 2011), is at the crossroads of these emerging mechanisms. On the one hand, p114RhoGEF mediates Gαβγ-dependent junctional contractility in *Drosophila*, *Xenopus*, or mammalian cells presumably via RhoA (Acharya et al., 2018; Garcia De Las Bayonas et al., 2019; Marivin and Garcia-Marcos, 2019; Silver et al., 2019). On the other hand, p114RhoGEF also interacts with PAR3 to mediate the remodeling of the apical actin cytoskeleton (Nakajima and Tanoue, 2011; Terry et al., 2011). Our observations reported here suggest that DAPLE may serve as a G protein–p114RhoGEF activating input that is spatially restricted to apical junctions via PAR polarity complex association.

Intriguingly, DAPLE was originally identified as an interacting partner of Disheveled (Oshita et al., 2003), which is a component of the planar cell polarity (PCP) core machinery (Butler and Wallingford, 2017). In fact, it has been proposed that DAPLE and Disheveled, which colocalize at the same side of planar polarized MCCs, might coordinately regulate polarized microtubule dynamics to control cilia organization and beating (Nakayama et al., 2021; Takagishi et al., 2020; Takagishi et al., 2017). Thus, the findings presented in our work raise two interesting ideas that remain to be investigated. The first is that, by associating with different types of polarity complexes, DAPLE might play a role in the interplay between them. Although there is precedent in the literature about the interplay between the PAR and PCP complexes in epithelial biology (Chuykin et al., 2018; Donati et al., 2021; Landin Malt et al., 2019), the precise mechanisms involved remain a mystery. The second interesting idea is that DAPLE may regulate not only polarized microtubule dynamics in MCCs, but also polarized actomyosin regulation. Given that both microtubule and actin apical networks are essential for cilia assembly and function (Antoniades et al., 2014; Tateishi et al., 2017; Werner et al., 2011), further investigation of the role of DAPLE in MCCs is warranted.

In summary, we have dissected a molecular mechanism that directly links polarity complexes at cell–cell junctions with remodeling of the actin cytoskeleton at the apical domain of epithelial cells, which may have broad implications for the biology of numerous tissues and organs.

Materials and methods

Plasmids

Plasmids for virus packaging were pMD2.G (#12259; Addgene) and psPAX2 (#12260; Addgene). Plasmids for the expression of shRNAs were constructed by insertion of a hairpin sequence, generated by annealing of complementary primers, into pLKO.1-puro plasmid (#8453; Addgene) at AgeI/EcoRI sites. The shRNA hairpins used were the following (target sequence is underlined and hairpin loop is italicized): dog PAR3 (shPAR3, 5′-CCGGGGATAAAGCTGGCAAAGA*CTCGAG*TCTTTGCCAGCTTTATCCTTTTTG-3′; Chen and Macara, 2005), dog DAPLE (sh1DAPLE, 5′-CCGGGACCATCTTGGTGAGAAATAT*CTCGAG*ATATTTCTCACCAAGATGGTCTTTTTG-3′; sh5DAPLE, 5′-CCGGCATCGAGCTGGAGCGGAATAA*CTCGAG*TTATTCCGCTCCAGCTCGATGTTTTTG-3′), mouse DAPLE (sh2DAPLE, 5′-CCGGTGGCCGCACCAAAGGTTGTAAT*CTCGAG*ATTACAACCTTTGGTGCGGCCTTTTTG-3′; sh3DAPLE, 5′-CCGGTGCAGCTGATCGTAATGAATTT*CTCGAG*AAATTCATTACGATCAGCTGCTTTTTG-3′); and a control hairpin not targeting host sequences (shCtrl, 5′-CCGGTGGAGTACAACTACAACAGCCA*CTCGAG*TGGCTGTTGTAGTTGTACTCCATTTTTG-3′).

The plasmid for the stable expression of human MYC-DAPLE in mammalian cells (full length, pLVX-mVenus-MYC-DAPLE) was generated by Gibson assembly of mVenus (from pcDNA3-Venus-cpVenus-FLARE-AKAR; #123329; Addgene) and MYC-DAPLE (from pCS2-6XMYC-hDAPLE) into pLVX-IRES-Hyg (Clontech) at XhoI and NotI sites. Silent mutations were introduced in MYC-DAPLE to make it insensitive to silencing mediated by dog sh5DAPLE (mutated sequence was 5′-CATCGAATTAGAGAGGAATAA-3′; mismatches are underlined). Another plasmid used in Figs. 5 and S5 for expression of MYC-DAPLE in mammalian cells (pCS2-6XMYC-hDAPLE) has been described previously (Marivin et al., 2019). The plasmids for the expression of GST-DAPLE-CT (aa 1,650–2,028, pGEX-4T-1-DAPLE-CT), GST-DAPLE-CT1 (aa 1,650–1,745, pGEX-4T-1-DAPLE-CT1), GST-xDAPLE (aa 1,648–1,704, pLIC-GST-xDAPLE GBA1 + GBA2), and His-DAPLE-CT (aa 1,650–2,028, pET28b-DAPLE) in bacteria have been described previously (Aznar et al., 2015; Marivin et al., 2020; Marivin et al., 2019). The plasmid for the expression of GST-DAPLE-CT2 (aa 1,746–2,028, pLIC-GST-DAPLE-CT2) was generated by ligation-independent cloning (LIC; Stols et al., 2002) into pLIC-GST (kindly provided by J. Sondek, University of North Carolina-Chapel Hill, Chapel Hill, NC; Cabrita et al., 2006). All point mutations in DAPLE (ΔPBM, GBA*, and SH3-BM*) were generated by site-directed mutagenesis using QuikChange II (Agilent) following the manufacturer's instructions.

Plasmids for the expression of human FLAG-PAR3 (pEXPR-FLAG-PAR3A), FLAG-PKCζ (pEXPR-3xFLAG-PKCζ), and FLAG-PAR6 (pEXPR-3xFLAG-PAR6A) were kindly provided by Xaralabos (Bob) Varelas (Boston University, Boston, MA). pEXPR plasmids were generated using the Gateway cloning system (Invitrogen) to

insert the sequences of the human genes in a destination vector with a CMV promoter and an in-frame FLAG or 3xFLAG sequence at the N-terminal end of the insert. The plasmid for the expression of GFP-PAR3N (pCS2-GFP-Par3N; Chuykin et al., 2018) was a gift from S. Sokol (Icahn School of Medicine at Mount Sinai, New York, NY). Plasmids for the expression of AHPH-GFP (pEGFP-RhoA Biosensor, Addgene #68026; Piekny and Glotzer, 2008) and for AHPH-GFP DM mutant (GFP-AHPH-DM, Addgene #71368; Priya et al., 2015) were purchased from Addgene. Plasmids for the expression of FLAG-CD2AP (pFLAG-CMV-2-CD2AP) in mammalian cells or of GST-p130Cas-SH3 (pGEX-2-TK-p130Cas-SH3), GST-CD2AP-SH3-1 (pGEX-4T-3-CDAP2-SH3-1), GST-CD2AP-SH3-2 (pGEX-GP-1-CDAP2-SH3-1), GST-CD2AP-SH3-3 (pGEX-KN-CDAP2-SH3-3), and GST-Yes-SH3 (pGEX-Yes-SH3) in bacteria were kindly provided by Kathrin Kirsch (Boston University, Boston, MA; Kirsch et al., 1999). The plasmids for the expression of GST-Nck-SH3-N (pGEX-4T3-hNck-NSH3), GST-Nck-SH3-M (pGEX-4T3-hNCK-MSH3), GST-Nck-SH3-C (pGEX4T3-hNCK-CSH3), GST-Crk-SH3-N (pGEX2T-hCrk-NSH3), GST-Crk-SH3-C (pGEX2T-hCrk-CSH3), GST-Grb2-SH3-N (pGEX4T2-mGrb2-NSH3), GST-Grb2-SH3-C (pGEX2T-hGrb2-CSH3), GST-Lyn-SH3 (pGEX4T3-mLynSH), GST-cSrc-SH3 (pGEX4T3-cSrcSH3), and GST-Abl-SH3 (pGEX3X-hAblSH3) in bacteria were a gift from C. Li (University of Western Ontario, London, Canada; Jia et al., 2005). The plasmid for the expression of GST-Gαi3 (pGEX-KG-Gαi3) has been described previously (Ghosh et al., 2008). Plasmids for the expression of GST-PAR3 (PDZ1-3; aa 252–697, pLIC-GST-PAR3-PDZ1-3) and MBP-PAR3 (PDZ1-3; aa 252–697, pLIC-MBP-PAR3-PDZ1-3) were generated by LIC cloning (Stols et al., 2002). Plasmids for the expression of membrane RFP (pCS2-mRFP) and GFP-CAAX (pCS2-eGFP-CAAX) in *Xenopus* were a gift from S. Sokol (Icahn School of Medicine at Mount Sinai, New York, NY; Ossipova et al., 2014).

General cell culture, lentivirus packaging, and generation of stable cell lines

HEK293T (CRL3216; American Type Culture Collection [ATCC]), Lenti-X 293T (#632180; Takara Bio), MDCK (CRL2936; ATCC), and Eph4 (CRL3071; ATCC) cells were grown at 37°C, 5% (vol:vol) CO_2 in DMEM supplemented with 10% (vol:vol) FBS, 100 U/ml penicillin, 100 µg/ml streptomycin, and 2 mM L-glutamine.

Lentiviruses were produced by transfection of Lenti-X 293T cells using polyethylenimine (PEI; #23966; Polysciences; 1-mg/ml solution reconstituted in water). 500,000 cells were seeded per well of a 6-well plate and cotransfected the next day with lentiviral plasmid of interest (1.8 µg), packaging plasmids psPAX2 (1.2 µg), and pMD2.G (0.75 µg). Plasmid DNA was added to 100 µl of OptiMEM and mixed with 7.5 µl of PEI reagent by vortexing for 2 s. Tubes were incubated at room temperature for 15 min before adding to cells. 18 h after transfection, the medium was changed, and ∼42 h later, lentivirus-containing media were collected, centrifuged at 500 *g* for 3 min, and filtered through a 0.45-µm polyethersulfone membrane filter.

For the generation of MDCK and Eph4 cell lines stably expressing shRNAs, cells were seeded on 6-well plates (200,000 cells per well). The day after seeding, cells were transduced by 24-h incubation with 2 ml of a 1:1 mix of lentivirus-containing supernatants described above mixed with fresh complete medium and supplemented with 10 µg/ml of polybrene. Cells were transferred to a 10-cm plate, and selection with 5 µg/ml puromycin started the day after. All surviving clones were pooled and maintained in the presence of 2.5 µg/ml puromycin. For the expression of MYC-DAPLE constructs in MDCK sh5DAPLE cells, cells were transduced as described above and selected with 200 µg/ml of hygromycin B. Surviving clones were pooled and maintained in the presence of 100 µg/ml hygromycin B and 2.5 µg/ml puromycin.

TEER measurements

80,000 MDCK cells were seeded on 24-well Transwell inserts (#3470; Corning). For calcium switch experiments, cells were grown for 6 d, washed three times with PBS, and incubated for 18 h in medium with reduced calcium consisting of MEM medium without calcium (M8167; Sigma-Aldrich) and 10% (vol:vol) FBS dialyzed overnight at 4oC against PBS with a 10,000-D cutoff membrane (#88243; Thermo Fisher Scientific). After replacing the medium with complete calcium-containing medium (DMEM supplemented with 10% [vol:vol] FBS, 100 U/ml penicillin, 100 µg/ml streptomycin, and 2 mM L-glutamine), TEER measurements were carried out at the indicated times with a Millicell ERS-2 system (Millipore) at room temperature and corrected by subtraction of the electrical resistance measured in an empty Transwell filter chamber filled with complete medium. Final corrected TEER values were expressed as ohm/cm^2. In some cases, filters were withdrawn at specific time points and processed for staining as described in Immunofluorescence of cells seeded on polycarbonate filters.

For experiments testing the effect of CalA on TEER (Fig. 1 H), cells were seeded as above and grown for 8 d. Cells were treated with 80 nM CalA (#9902S; Cell Signaling Technology), and TEER measurement at specific time points was carried out as described above.

Immunofluorescence staining of cells seeded on polycarbonate filters

For immunofluorescence stainings shown in Fig. 1, C–G; Fig. 2, B and C; Fig. 3, A–H; Fig. 6, C and D; Fig. S1 G; Fig. S2; Fig. S3 B; and Fig. S4, B–F, MDCK cells were seeded on polycarbonate Transwell filters at a density of 80,000 cells per well in 24-well plate inserts (#3470; Corning) and grown for 8 d before fixation. For immunofluorescence stainings shown in Fig. 7, B–G; Fig. S3 A; and Fig. S5, E and F, MDCK cells were processed exactly as described above except that different polycarbonate Transwell filters were used (Thincerts #662640; Greiner Bio-One) because of shortages of the product above.

For experiments shown in Fig. S3 A, 500,000 MDCK cells were seeded in 6-well plates and transfected the next day with a mixture containing 2 µg plasmid DNA encoding AHPH-GFP and 4 µl Turbofect (R0531; Thermo Fisher Scientific) in 200 µl OptiMEM prepared following the manufacturer's instructions. The next day, cells were seeded on polycarbonate Transwell filters (24-well inserts) at a density of 100,000 cells per well and grown for 6 d.

For experiments involving pharmacological treatments, MDCK cell monolayers were treated with 80 nM CalA (#9902S;

Cell Signaling Technology) for 20 min at 37°C before fixation. In some cases, this treatment was preceded by preincubation with 10 µM Y-27632 (#1254; Tocris) for 30 min, or with 50 µM Blebbistatin (sc-203532B; Santa Cruz Biotechnology) for 1 h at 37°C. Controls received an equivalent volume of DMSO. Latrunculin B (#428020; EMD) was used at 10 µM for 2 h at 37°C.

Unless otherwise indicated, cell monolayers were washed gently one time with PBS containing Ca^{2+} and Mg^{2+} at room temperature, fixed with 4% (wt:vol) PFA in fixation buffer (10 mM Pipes, pH 6.8, 100 mM KCl, 300 mM sucrose, 2 mM EGTA, and 2 mM $MgCl_2$) for 10 min at 4°C, and washed three times for 5 min with PBS. For RhoA stainings, cells were fixed in 10% TCA diluted in water for 15 min at 4°C and washed three times in PBS supplemented with 30 mM glycine. For CD2AP and DAPLE stainings, cells were fixed in ice-cold methanol for 10 min at −20°C and washed three times for 5 min with PBS. For all stainings, cells were permeabilized for 5 min with 0.25% (vol:vol) Triton X-100 in PBS and blocked for 1 h in blocking buffer (5% [vol:vol] goat serum and 0.1% [vol:vol] Triton X-100 in PBS). At that point, filters were excised from the Transwell with a razor blade and further cut into two or four pieces. Filter membranes were placed upside down over 30 µl primary antibody solution spotted on parafilm and incubated overnight at 4°C in a humid chamber. Primary antibodies were diluted in blocking buffer as follows: PAR3 (rabbit; #07-330, 1:400; Millipore), ZO-1 (rabbit; #61-7300, 1:500; Invitrogen), ZO-1 (rat; R26.4c, 1:500; DHSB), E-cadherin (mouse; rr1, 1:200; DHSB), Podocalyxin (mouse, DHSB 3F2D8, 1:50), β-catenin (mouse; #610153, 1:200; BD Transduction Laboratories), β-catenin (rabbit, ab1605, 1 1:500; Abcam), DAPLE (rabbit; ABS515, 1:200; Millipore), NMIIB (rabbit; #9099, 1:100; BioLegend), RhoA (mouse; sc-418, 1:100; Santa Cruz Biotechnology), PP-MLC2 (rabbit; #3674, 1:100; Cell Signaling Technology), YAP/TAZ (rabbit; #8418, 1:200; Cell Signaling Technology), and CD2AP (mouse; sc-25272, 1:50; Santa Cruz Biotechnology). Filters were washed three times for 5 min in PBS at room temperature, placed upside down over 30 µl secondary antibody solution spotted on parafilm, and incubated for 1 h at room temperature in a humid chamber. The following secondary antibodies (Life Technologies) were diluted in blocking buffer as follows: goat anti-mouse Alexa Fluor 488 (1:400; A11017), goat anti-rabbit Alexa Fluor 488 (1:400; A11070), goat anti-mouse Alexa Fluor 594 (1:400; A11020), goat anti-rabbit Alexa Fluor 594 (1:400; A11072), and goat anti-rat Alexa Fluor 647 (1:400; A21247). For experiments staining for F-actin, Alexa Fluor 488–conjugated phalloidin (PHDG1-A; Cytoskeleton) was included along secondary antibodies at 70 nM after drying of methanol stocks and resuspension in aqueous buffer at the time of the experiment. Next, filters were stained with DAPI (1:10,000) for 5 min at room temperature, washed three times for 5 min with PBS at room temperature, and mounted in ProLong Diamond Antifade (P36965; Invitrogen) before imaging as described in Fluorescence microscopy.

Immunofluorescence staining of cells seeded on Matrigel

For experiments with 3D cultures, 15,000 MDCK cells per well were seeded in 8-well Lab-Tek II chamber slides (#154534; Thermo Fisher Scientific) coated with Matrigel (#356234; Corning), as described previously (Debnath et al., 2003), and grown for 4 d in DMEM (vol:vol) supplemented with 10% FBS, 2% (vol:vol) Matrigel, 100 U/ml penicillin, 100 µg/ml streptomycin, and 2 mM L-glutamine. Cells were washed once with PBS containing Ca^{2+} and Mg^{2+} at room temperature and fixed for 30 min at room temperature with 4% (wt:vol) PFA diluted in PBS. Cells were washed with PBS three times for 10 min at room temperature and incubated in permeabilization solution (0.5% [vol:vol] Triton X-100 and 3% [wt:vol] BSA in PBS) for 1 h at room temperature. Cells were then incubated overnight at room temperature with primary antibodies for β-catenin (rabbit; ab1605, 1:200; Abcam) and Podocalyxin (mouse; 3F2D8, 1:40; DHSB) diluted in blocking solution (0.5% [vol:vol] Triton X-100, 3% [wt:vol] BSA, and 5% [vol:vol] goat serum in PBS). Cells were washed three times for 20 min with PBS at room temperature and then incubated with secondary antibodies as described in Immunofluorescence staining of cells seeded on polycarbonate filters. Cells were washed three times for 10 min with PBS at room temperature and stained with DAPI (1:10,000) for 20 min at room temperature. After one wash with PBS, cultures were mounted in ProLong Diamond Antifade and cured overnight at room temperature before imaging.

Immunofluorescence staining of cells seeded on coverslips

For immunofluorescence stainings shown in Fig. 2 D; Fig. 4, A and B; Fig. S1 C; and Fig. S1, I–K, cells were seeded on glass coverslips placed in a 24-well plate at a density of 120,000 cells per well for Eph4 or 250,000 cells per well for MDCK and grown for 2 d before fixation. For PAR3 knock-down experiments shown in Fig. 2 F, MDCK cells were seeded on glass coverslips placed in 24-well plates at a density of 80,000 cells per well. The next day, cells were treated with supernatants containing shPAR3 or shCtrl lentivirus (mixed 1:1 with fresh medium containing 10 µg/ml of polybrene) for 1 d, and cells were grown for four more days, replacing the medium every day. For experiments shown in Fig. 2 G with GFP-PAR3N, cells were transfected the day after seeding with a mixture containing 1 µg plasmid DNA encoding GFP-PAR3N and 2 µl Turbofect (R0531; Thermo Fisher Scientific) in 100 µl OptiMEM prepared following the manufacturer's instructions and grown for 30 h before fixation.

Unless otherwise indicated, cell monolayers were fixed in ice-cold methanol for 10 min at −20°C and washed three times for 5 min with PBS at room temperature. For the F-actin, NMIIB, and PP-MLC2 staining, cells were washed with PBS containing Ca^{2+} and Mg^{2+} at room temperature and fixed with 4% (wt:vol) PFA in fixation buffer (10 mM Pipes, pH 6.8, 100 mM KCl, 300 mM sucrose, 2 mM EGTA, and 2 mM $MgCl_2$) for 10 min at 4°C. Cells were washed three times for 5 min with PBS and permeabilized for 5 min with 0.25% (vol:vol) Triton X-100 in PBS. For all staining, cells were incubated at room temperature for 1 h in blocking buffer (5% [vol:vol] goat serum and 0.1% [vol:vol] Triton X-100 in PBS). Coverslips were placed upside down over 30 µl primary antibody solution spotted on parafilm and incubated overnight at 4°C in a humid chamber. Primary antibodies were diluted in blocking buffer as follows: DAPLE (rabbit; ABS515, 1:200; Millipore), PAR3 (mouse; MAB8030, 1:100; R&D

Systems), ZO-1 (rat; DHSB R26.4c, 1:500), ZO-1 (rabbit; #61-7300, 1:500; Invitrogen), GFP (mouse; sc-9996, 1:200; Santa Cruz Biotechnology), β-catenin (rabbit; ab1605, 1 1:500; Abcam), CD2AP (mouse; sc-25272, 1:50; Santa Cruz Biotechnology), NMIIB (rabbit; #9099, 1:100; BioLegend), RhoA (mouse; sc-418, 1:100; Santa Cruz Biotechnology), and PP-MLC2 (rabbit; #3674, 1:100; Cell Signaling Technology). Coverslips were washed three times for 5 min and incubated in secondary antibodies or Alexa Fluor 488–conjugated phalloidin (PHDG1-A; Cytoskeleton) at 70 nM after drying of methanol stocks and resuspension in aqueous buffer at the time of the experiment. Coverslips were mounted as described in Immunofluorescence staining of cells seeded on polycarbonate filters before imaging as described in Fluorescence microscopy.

Fluorescence microscopy

Wide-field microscopy imaging was performed at room temperature with a Zeiss Axio Observer Z1 microscope equipped with a digital camera (C10600/ORCA-R2 Hamamatsu Photonics). Images were taken with a 63x oil-immersion objective (NA 1.4; working distance 0.19 mm) using Zen software. Confocal microcopy analysis was carried out at room temperature with a Zeiss LSM 700. Stacks of confocal images of 0.321-µm thickness along the z axis were taken with a 63x oil-immersion objective (NA 1.4, working distance 0.19 mm) using Zen software. Maximum-intensity projections, brightness/contrast adjustments, and image exports were performed using Zen software. Individual images were assembled for presentation in Photoshop and Illustrator software (Adobe).

Quantification of apical area and linearity index of apical cell–cell junctions

Quantification of the apical area and linearity index of apical cell–cell junctions were calculated from wide-field fluorescence microscopy pictures of cell monolayers stained for ZO-1 to delineate the apical cell boundaries. For apical area measurements, images were segmented using the segmentation tool of Tissue Analyzer plugin in ImageJ (Aigouy et al., 2010), followed by visual inspection and manual correction as needed. After segmentation, individual cell areas, excluding border cells, were determined using the plots tool of the Tissue Analyzer plugin. Linearity index of apical cell–cell junctions was determined by dividing the distance between the cell junction vertices (obtained by using the straight line tool of ImageJ) by the cell junction length (obtained using the freehand drawing tool of ImageJ).

Quantification of fluorescence intensity

Quantification of junctional fluorescence intensity for Fig. 2, F and G; Fig. 3, C–G; Fig. 4 A; Fig. 7, E–G; Fig. S1, I–K; Fig. S4, B and C; and Fig. S5 F was performed using the linescan analysis tool of ImageJ. This analysis was carried out on wide-field pictures or maximum-intensity projections from confocal images for Fig. 2, F and G (as indicated in the figure legend) and on single optical sections for Fig. 3, C–G; Fig. 4 A; Fig. 7, E–G; Fig. S1, I–K; Fig. S4, B and C; and Fig. S5 F. A line of 10-µm length and 2-µm width was drawn perpendicular to and centered on each bicellular junction analyzed, and fluorescence intensity along the line was extracted using plot profile and transferred to an Excel file. Each profile was corrected by subtracting the baseline fluorescence intensity determined by averaging the values from 3 µm at both ends of the profile. Then, baseline-corrected peak values (maximum) from the central region of the baseline-corrected profile were taken as the junctional fluorescence intensities. To be able to average results across different experiments with varying overall fluorescence intensities, fluorescence intensity values calculated above were normalized to the mean value of a control group in each experiment and expressed as normalized arbitrary fluorescence units (n.a.f.u.).

Quantification of junctional fluorescence intensity for F-actin (Figs. 3 B and 7 C) was carried out by drawing a box of 2 × 2 µm centered on apical cell–cell junctions (positioned using PAR3 costaining) on single optical sections. The average fluorescence intensity per cell–cell boundary was baseline corrected by subtracting an average intensity value from a box placed in the center of the medial plane of the same cell. Quantification of F-actin intensity at basal or apical levels (Figs. 3 B and 8 F) was carried out by using the freehand tool of ImageJ to draw areas that encircled the whole cell (including cell–cell junctions) on single optical sections. The average fluorescence intensity per cell was baseline corrected as described for the quantification of F-actin junctional fluorescence intensity. Results were processed to be expressed as n.a.f.u. as described above. Quantification of junctional fluorescence intensity of AHPH-GFP (Fig. S3 A) was carried out by drawing freehand lines of 2-µm thickness centered on apical cell–cell junctions (positioned using ZO-1 costaining) on maximum-intensity projections from confocal images. The average fluorescence intensity along this line (junctional intensity) was divided by the average intensity value from a box placed in the center of the cell (cytoplasmic intensity), and results were normalized to the mean value of the control group in each experiment.

To calculate the distribution of E-cadherin and ZO-1 at cell–cell junctions (Fig. 1 E), linescan analysis and baseline corrections on maximum-intensity projections from confocal z stacks were performed as described above for the quantification of junctional fluorescence intensity. Results were presented as the distribution of signals across the 10-µm length of each profile by taking baseline-corrected fluorescence intensities at each point and calculating the percentage relative to the sum of intensities for the entire profile. Fluorescence intensity profile of DAPLE and CD2AP (Fig. 4 B), was carried by linescan analysis (1-µm thickness) along the magnified cell–cell junctions depicted in the figure.

Immunoprecipitation

Approximately 2.2 million HEK293T cells were seeded on 10-cm dishes and transfected the day after with plasmids encoding MYC-DAPLE (6 µg), FLAG-PAR3 (4 µg), FLAG-PAR6 (1 µg), and/or FLAG-PKCζ (1 µg), as indicated in the figure, using PEI. Total DNA amount was equalized to 12 µg using pcDNA3.1(+). Plasmid DNA was added to 500 µl DMEM and mixed with 30 µl PEI reagent by vortexing for 2 s. Tubes were incubated at room temperature for 15 min before adding to cells, and medium was

changed 6 h later. 24 h after transfection, cells were lysed on ice with 600 µl lysis buffer (20 mM Hepes, pH 7.2, 5 mM Mg $[CH_3COO]_2$, 125 mM K$[CH_3COO]$, 0.4% [vol:vol] Triton X-100, 1 mM DTT, 10 mM β-glycerophosphate, and 0.5 mM Na_3VO_4 supplemented with a protease inhibitor cocktail [S8820; Sigma-Aldrich]) and cleared (14,000 *g*, 10 min). Cleared lysates were incubated with 1.5 µg rabbit anti-MYC antibodies (C3956; Sigma-Aldrich) for 2.5 h at 4°C with constant rotation. 30 µl of a ∼50% protein A agarose bead suspension, preblocked with 5% (wt:vol) BSA in PBS for 2 h at room temperature, was added to the lysate:antibody mixture and incubated for 90 min at 4°C. Beads were washed 3 times at 1,000 *g* for 30 s with wash buffer (4.3 mM Na_2HPO_4, 1.4 mM KH_2PO_4, pH 7.4, 137 mM NaCl, 2.7 mM KCl, 0.1% [vol:vol] Tween-20, 10 mM $MgCl_2$, 5 mM EDTA, and 1 mM DTT), and proteins were eluted by boiling in Laemmli sample buffer for 5 min. Proteins were separated by SDS-PAGE and immunoblotted with antibodies as indicated in Preparation of cell lysates and immunoblotting.

Preparation of cell lysates and immunoblotting

For the analysis of total protein levels shown in Figs. 1 A, 2 A, 6 B, and S1 B, MDCK cells were seeded on 6-well plates at a density of 800,000 cells per well and grown for 2 d before lysis. Cells were washed once with PBS and lysed in ice with 200 µl of lysis buffer (20 mM Hepes, pH 7.2, 5 mM Mg$[CH_3COO]_2$, 125 mM K$[CH_3COO]$, 0.4% [vol:vol] Triton X-100, 1 mM DTT, 10 mM β-glycerophosphate, and 0.5 mM Na_3VO_4 supplemented with a protease inhibitor cocktail [S8820; Sigma-Aldrich]). Lysates were syringed 10 times through a 30-gauge needle and kept on ice for 30 min before adding Laemmli sample buffer and boiling for 5 min.

For the analysis of total protein levels shown in Figs. 4 A, S1 F, and S4 G, MDCK cells were seeded on polycarbonate filters (6-well Transwell insert; #3450; Corning) at a density of 320,000 cells per well and grown for 8 d. For experiments shown in Fig. S4 G, cells were treated with 80 nM CalA for 20 min at 37°C. Cells were washed once with PBS at room temperature and then lysed on ice for 30 min after adding 200 µl RIPA buffer (20 mM Tris-HCl, pH 7.4, 150 mM NaCl, 1% [vol:vol] NP-40, 0.5% [wt:vol] sodium deoxycholate, 0.1% [wt:vol] SDS, 10 mM β-glycerophosphate, 0.5 mM Na_3VO_4, 1 mM DTT, and a protease inhibitor cocktail [S8820; Sigma-Aldrich]). Lysates were cleared (14,000 *g*, 10 min) before adding Laemmli sample buffer and boiling for 5 min.

Proteins were separated by SDS-PAGE and transferred to polyvinylidene difluoride membranes, which were blocked with 5% (wt:vol) nonfat dry milk in Tris-buffered saline solution supplemented with 0.1% [wt:vol] Tween-20 (TBS-T) and sequentially incubated with primary and secondary antibodies. For protein–protein binding experiments with GST-fused proteins, polyvinylidene difluoride membranes were stained with Ponceau S and scanned before blocking. The following primary antibodies were diluted in 5% (wt:vol) nonfat dry milk TBS-T: DAPLE (rabbit; ABS515, 1:1,000; Millipore), FLAG (mouse; F1804, 1:2,000; Sigma-Aldrich), MYC (mouse; #2276, 1:1,000; Cell Signaling Technology), His (mouse; H10, 1:2,500; Sigma-Aldrich), Tubulin (mouse; T6074, 1:2,500; Sigma-Aldrich), β-actin (rabbit; C80813, 1:2,000; Li-Cor Biosciences), ZO-1 (rabbit; #61-7300, 1:1,000; Zymed), E-cadherin (mouse; rr1, 1:1,000; DHSB), β-catenin (mouse; #610153, 1:1,000; BD Transduction Laboratories), PAR3 (rabbit; #07-330, 1:1,000; Millipore), PKCζ (rabbit; sc-216, 1:1,000; Santa Cruz Biotechnology), and xDAPLE (rabbit; 1:1,000). The rabbit polyclonal antibody for xDAPLE was custom made using GST-xDAPLE GBA1 + GBA2 (aa 1,648–1,704) as antigen. The other antibodies indicated below were diluted in 2% (wt:vol) BSA in TBS-T: PATJ (rabbit; provided by A. Le Bivic [Aix-Marseille University], 1:1,000) and CD2AP (rabbit; sc-9137, 1:500; Santa Cruz Biotechnology). The secondary antibodies were diluted in 5% (wt:vol) nonfat dry milk TBS-T as follows: goat anti-rabbit Alexa Fluor 680 (A21077, 1:10,000; Invitrogen) and goat anti-mouse IRDye 800 (#926-32210, 1:10,000; Li-Cor Biosciences). Infrared imaging of immunoblots was performed using an Odyssey Infrared Imaging System (Li-Cor Biosciences).

Protein expression in bacteria and purification

His-tagged, GST-tagged, and maltose binding protein (MBP)–tagged proteins were expressed in BL21(DE3) transformed with the corresponding plasmids by overnight induction at 23°C with 1 mM IPTG. For MBP-tagged proteins, bacterial medium was supplemented with 0.2% (vol:vol) glucose. Protein purification was carried out following previously described protocols (Garcia-Marcos et al., 2009). Briefly, bacteria pelleted from 1 liter of culture were resuspended in 25 ml of buffer (50 mM NaH_2PO_4, pH 7.4, 300 mM NaCl, 10 mM imidazole, and 1% [vol:vol] Triton X-100 supplemented with protease inhibitor cocktail [1 µM leupeptin, 2.5 µM pepstatin, 0.2 µM aprotinin, and 1 mM phenylmethylsulfonyl fluoride]). After sonication (4 cycles, with pulses lasting 20 s/cycle, and with a 1-min interval between cycles to prevent heating), lysates were centrifuged at 12,000 *g* for 20 min at 4°C. The soluble fraction (supernatant) of the lysate was used for affinity purification on HisPur cobalt (#89964; Thermo Fisher Scientific), glutathione agarose (#16100; Thermo Fisher Scientific), or amylose resins (E8021; New England Biolabs). Elutions were carried out with lysis buffer supplemented with 250 mM imidazole for His-tagged proteins or with 50 mM Tris-HCl, pH 8, 100 mM NaCl, and 30 mM reduced glutathione for GST-tagged proteins. For MBP-tagged proteins, elutions were performed in 20 mM Tris-HCl, pH 7.5, 200 mM NaCl, 1 mM EDTA, and 10 mM Maltose. Proteins were dialyzed overnight at 4°C against PBS with a 10,000 D cutoff membrane (#88243; Thermo Fisher Scientific). All protein samples were aliquoted and stored at −80°C.

In vitro protein-binding assays with GST-fused proteins

GST-fused DAPLE fragments (30 µg), GST-SH3 fragments (30 µg), GST-Gαi3 (10 µg), GST-PAR3 (15 µg), or a matching amount of GST protein (control) were immobilized on glutathione-agarose beads for 90 min by incubation with tumbling in ∼500 µl of PBS at room temperature. Beads were washed twice with PBS and resuspended in 300 µl binding buffer (50 mM Tris-HCl, pH 7.4, 100 mM NaCl, 0.4% [vol:vol] NP-40, 10 mM $MgCl_2$, 5 mM EDTA, and 1 mM DTT) before adding the soluble ligands to start the binding reactions.

For experiments using cell lysates as a source of soluble ligands, 2 million HEK293T cells were seeded on 10-cm dishes and

transfected the next day with plasmids encoding FLAG-CD2AP (6 µg) or MYC-DAPLE (12 µg) using the calcium phosphate method. 30 h after transfection, cells were lysed at 4°C in 500 µl lysis buffer (20 mM Hepes, pH 7.2, 5 mM $Mg[CH_3COO]_2$, 125 mM $K[CH_3COO]$, 0.4% [vol:vol] Triton X-100, 1 mM DTT, 10 mM β-glycerophosphate, and 0.5 mM Na_3VO_4 supplemented with a protease inhibitor cocktail [#78430; Thermo Fisher Scientific]). Lysates were cleared at 14,000 *g* for 10 min, and 100 µl of lysate was added to each tube with GST-fused proteins immobilized on resin, followed by incubation for 4 h at 4°C with constant tumbling. Beads were washed four times with 1 ml of wash buffer (4.3 mM Na_2HPO_4, 1.4 mM KH_2PO_4, pH 7.4, 137 mM NaCl, 2.7 mM KCl, 0.1% [vol:vol] Tween-20, 5 mM EDTA, and 1 mM DTT), and resin-bound proteins were eluted by boiling in Laemmli sample buffer for 5 min. Proteins were separated by SDS-PAGE and immunoblotted as indicated in the figures. For experiments using purified proteins as soluble ligands, stocks of purified proteins were thawed and centrifuged at 14,000 *g* for 2 min before adding to the tubes with GST proteins. Quantities of purified proteins added in each tube were 1.5 µg of His-DAPLE-CT for Fig. 5 D and 4 µg of His-DAPLE-CT and/or 4 µg of MBP-PAR3 (PDZ1-3) for Fig. S5 G. The remaining steps were carried out as in the experiments with cell lysates, except for Fig. S5 G, for which proteins were analyzed by Coomassie staining.

Xenopus experiments

Frog studies were performed with WT Xenopus animals (Nasco) according to Boston University Institutional Animal Care and Use Committee–approved protocol AN14092, in compliance with the Guide for the Care and Use of Laboratory Animals. Egg laying was induced by dorsal lymph injection of 600 U of human chorionic gonadotrophin (Chorulon; Merck). In vitro fertilization and embryo culture were performed in 0.1× Marc's modified Ringer's medium as previously described (Newport and Kirschner, 1982). Dejellied embryos from at least three independent frog fertilizations were used in all of the experiments. The following MOs were purchased from Gene Tools: xDAPLE MO targeting xDAPLE (transcription start site −1/+24 nt: 5′-CTG TTGGGAAATGGTAGTATCCATG-3′; Kobayashi et al., 2005; Marivin et al., 2019) and control MO (5′-CCTCTTACCTCAGTT ACAATTTATA-3′). mRNAs for injections in frog embryos were prepared using the SP6 mMessage mMachine Kit (AM1340; Ambion). MOs and mRNAs were injected in two animal blastomeres at the 4-cell stage to target the epidermis. Each blastomere was coinjected with 20 ng MOs and 50 pg mRNA encoding for mRFP or GFP-CAAX. Embryos were cultured at 16–22°C and fixed at stage 28 before immunostaining.

For xDAPLE stainings, embryos were fixed in 2% (wt:vol) TCA diluted in water for 30 min at room temperature and washed three times for 10 min in PBS containing 0.3% (vol:vol) Triton X-100. For F-actin stainings, embryos were fixed in 4% PFA diluted in PBS for 90 min at room temperature and washed three times for 10 min in PBS containing 0.1% (vol:vol) Triton X-100. Embryos were incubated in blocking buffer (5% [vol:vol] goat serum and 0.1% [vol:vol] Triton X-100 in PBS) for 1 h at room temperature and incubated in the following primary antibodies diluted in blocking buffer overnight at 4°C: acetylated-tubulin (mouse; MABT868, 1:1,000; Sigma-Aldrich), ZO-1 (mouse; #33-9100, 1:400; Invitrogen), RFP (rabbit; ab62341, 1:400; Abcam), GFP (chicken; GFP-1010, 1:400; Aves), and xDAPLE (rabbit; 1:400). The rabbit polyclonal antibody for xDAPLE was custom made using GST-xDAPLE GBA1 + GBA2 (aa 1,648–1,704) as antigen. Embryos were washed 5 times for 45 min at room temperature in PBS containing 0.1% (vol:vol) Triton X-100. Embryos were next incubated in the following secondary antibodies diluted in blocking buffer overnight at 4°C: goat anti-rabbit Alexa Fluor 488 (1:400; A11070), goat anti-rabbit Alexa Fluor 594 (1:400; A11072), goat anti-mouse Alexa Fluor 647 (1:400; A21237), and goat anti-chicken Alexa Fluor 594 (1:400; A11042). For experiments staining for F-actin, Alexa Fluor 488–conjugated phalloidin (Cytoskeleton, PHDG1-A) was included along with secondary antibodies at 70 nM after drying of methanol stocks and resuspension in aqueous buffer at the time of the experiment. Embryos were washed five times for 45 min at room temperature in PBS containing 0.1% (vol:vol) Triton X-100 and mounted in Mowiol between two coverglasses (Werner and Mitchell, 2013). Embryos were analyzed by confocal microscopy as described in Fluorescence microscopy.

Statistical analysis

For experiments displaying pooled data, individual data points and/or mean ± SEM or ± SD are depicted. For other experiments, one representative result is presented. Datasets were subjected to a normality test (D'Agostino and Pearson omnibus normality test) calculated in GraphPad. For datasets that passed the normality test, statistical significance between various conditions was assessed by determining P values using ANOVA, with multiple comparison corrections as needed, in GraphPad. For datasets that did not pass the normality test, significance between various conditions was assessed by determining P values using the Mann–Whitney *U* test in GraphPad.

Online supplemental material

Fig. S1 shows that loss of DAPLE impairs junctional morphology and actomyosin without altering the localization or abundance of junctional and apicobasal polarity markers. Fig. S2 shows that MDCK cells stably depleted of PAR3 display disrupted apical cell junctions. Fig. S3 shows that loss of DAPLE decreases RhoA-GTP levels at apical cell junctions and favors YAP/TAZ nuclear localization. Fig. S4 shows that loss of DAPLE impairs CalA-induced accumulation of active myosin II at apical cell junctions. Fig. S5 shows an assessment of modular interactions of DAPLE with CD2AP and PAR3.

Acknowledgments

We thank I. Dominguez (Boston University) for providing equipment and expertise for experiments with *Xenopus*. We thank V. Trinkaus-Randall for giving access to the Confocal Microscopy Facility at Boston University School of Medicine. We thank S. Sokol (Icahn School of Medicine at Mount Sinai) and C. Li (University of Western Ontario) for plasmids and A. Le Bivic (Aix-Marseille University, Marseille, France) for the PATJ antibody. We also thank Xaralabos (Bob) Varelas for sharing

reagents and equipment. We thank Michael Blower (Boston University) and members of the Garcia-Marcos laboratory for critically appraising the manuscript draft.

This work was supported by National Institutes of Health grant R01GM136132.

The authors declare no competing financial interests.

Author contributions: A. Marivin performed and analyzed all experiments except for experiments in Fig. 2 G and Fig. S1 H, which were performed by R.X.-Y. Ho, and experiments in Fig. 2 E, which were performed by M. Garcia-Marcos. A. Marivin and M. Garcia-Marcos designed experiments. A. Marivin and M. Garcia-Marcos conceived the project and wrote the manuscript. M. Garcia-Marcos supervised the project.

Submitted: 2 November 2021
Revised: 28 January 2022
Accepted: 17 February 2022

References

Acharya, B.R., A. Nestor-Bergmann, X. Liang, S. Gupta, K. Duszyc, E. Gauquelin, G.A. Gomez, S. Budnar, P. Marcq, O.E. Jensen, et al. 2018. A mechanosensitive RhoA pathway that protects epithelia against acute tensile stress. *Dev. Cell*. 47:439–452.e6. https://doi.org/10.1016/j.devcel.2018.09.016

Acharya, B.R., S.K. Wu, Z.Z. Lieu, R.G. Parton, S.W. Grill, A.D. Bershadsky, G.A. Gomez, and A.S. Yap. 2017. Mammalian diaphanous 1 mediates a pathway for E-cadherin to stabilize epithelial barriers through junctional contractility. *Cell Rep.* 18:2854–2867. https://doi.org/10.1016/j.celrep.2017.02.078

Aigouy, B., R. Farhadifar, D.B. Staple, A. Sagner, J.C. Roper, F. Julicher, and S. Eaton. 2010. Cell flow reorients the axis of planar polarity in the wing epithelium of *Drosophila*. *Cell*. 142:773–786. https://doi.org/10.1016/j.cell.2010.07.042

Antoniades, I., P. Stylianou, and P.A. Skourides. 2014. Making the connection: Ciliary adhesion complexes anchor basal bodies to the actin cytoskeleton. *Dev. Cell*. 28:70–80. https://doi.org/10.1016/j.devcel.2013.12.003

Aznar, N., K.K. Midde, Y. Dunkel, I. Lopez-Sanchez, Y. Pavlova, A. Marivin, J. Barbazan, F. Murray, U. Nitsche, K.P. Janssen, et al. 2015. Daple is a novel non-receptor GEF required for trimeric G protein activation in Wnt signaling. *eLife*. 4:e07091. https://doi.org/10.7554/eLife.07091

Aznar, N., N. Sun, Y. Dunkel, J. Ear, M.D. Buschman, and P. Ghosh. 2017. A Daple-Akt feed-forward loop enhances noncanonical Wnt signals by compartmentalizing beta-catenin. *Mol. Biol. Cell*. 28:3709–3723. https://doi.org/10.1091/mbc.E17-06-0405

Bailles, A., C. Collinet, J.M. Philippe, P.F. Lenne, E. Munro, and T. Lecuit. 2019. Genetic induction and mechanochemical propagation of a morphogenetic wave. *Nature*. 572:467–473. https://doi.org/10.1038/s41586-019s4151492-9

Butler, M.T., and J.B. Wallingford. 2017. Planar cell polarity in development and disease. *Nat. Rev. Mol. Cell Biol.* 18:375–388. https://doi.org/10.1038/nrm.2017.11

Cabrita, L.D., W. Dai, and S.P. Bottomley. 2006. A family of *E. coli* expression vectors for laboratory scale and high throughput soluble protein production. *BMC Biotechnol.* 6:12. https://doi.org/10.1186/1472-6750

Carramusa, L., C. Ballestrem, Y. Zilberman, and A.D. Bershadsky. 2007. Mammalian diaphanous-related formin Dia1 controls the organization of E-cadherin-mediated cell–cell junctions. *J. Cell Sci.* 120:3870–3882. https://doi.org/10.1242/jcs.014365

Charras, G., and A.S. Yap. 2018. Tensile forces and mechanotransduction at cell–cell junctions. *Curr. Biol.* 28:R445–R457. https://doi.org/10.1016/j.cub.2018.02.003

Chartier, L., L.L. Rankin, R.E. Allen, Y. Kato, N. Fusetani, H. Karaki, S. Watabe, and D.J. Hartshorne. 1991. Calyculin-A increases the level of protein phosphorylation and changes the shape of 3T3 fibroblasts. *Cell Motil. Cytoskeleton* 18:26–40. https://doi.org/10.1002/cm.970180104

Chen, X., and I.G. Macara. 2005. Par-3 controls tight junction assembly through the Rac exchange factor Tiam1. *Nat. Cell Biol.* 7:262–269. https://doi.org/10.1038/ncb1226

Chesarone, M.A., A.G. DuPage, and B.L. Goode. 2010. Unleashing formins to remodel the actin and microtubule cytoskeletons. *Nat. Rev. Mol. Cell Biol.* 11:62–74. https://doi.org/10.1038/nrm2816

Choi, W., B.R. Acharya, G. Peyret, M.A. Fardin, R.M. Mege, B. Ladoux, A.S. Yap, A.S. Fanning, and M. Peifer. 2016. Remodeling the zonula adherens in response to tension and the role of afadin in this response. *J. Cell Biol.* 213:243–260. https://doi.org/10.1083/jcb.201506115

Chuykin, I., O. Ossipova, and S.Y. Sokol. 2018. Par3 interacts with Prickle3 to generate apical PCP complexes in the vertebrate neural plate. *eLife*. 7:e37881. https://doi.org/10.7554/eLife.37881

Coleman, B.D., A. Marivin, K. Parag-Sharma, V. DiGiacomo, S. Kim, J.S. Pepper, J. Casler, L.T. Nguyen, M.R. Koelle, and M. Garcia-Marcos. 2016. Evolutionary conservation of a GPCR-independent mechanism of trimeric G protein activation. *Mol. Biol. Evol.* 33:820–837. https://doi.org/10.1093/molbev/msv336

Costa, M., E.T. Wilson, and E. Wieschaus. 1994. A putative cell signal encoded by the folded gastrulation gene coordinates cell shape changes during *Drosophila* gastrulation. *Cell*. 76:1075–1089. https://doi.org/10.1016/0092-8674(94)90384-0

David, D.J., A. Tishkina, and T.J. Harris. 2010. The PAR complex regulates pulsed actomyosin contractions during amnioserosa apical constriction in *Drosophila*. *Development*. 137:1645–1655. https://doi.org/10.1242/dev.044107

de Opakua, A.I., K. Parag-Sharma, V. DiGiacomo, N. Merino, A. Leyme, A. Marivin, M. Villate, L.T. Nguyen, M.A. de la Cruz-Morcillo, J.B. Blanco-Canosa, et al. 2017. Molecular mechanism of Gαi activation by non-GPCR proteins with a Gα-binding and activating motif. *Nat. Commun.* 8:15163. https://doi.org/10.1038/ncomms15163

Debnath, J., S.K. Muthuswamy, and J.S. Brugge. 2003. Morphogenesis and oncogenesis of MCF-10A mammary epithelial acini grown in three-dimensional basement membrane cultures. *Methods*. 30:256–268. https://doi.org/10.1016/s1046-2023(03)00032-x

DiGiacomo, V., A. Marivin, and M. Garcia-Marcos. 2018. When heterotrimeric G proteins are not activated by G protein-coupled receptors: Structural insights and evolutionary conservation. *Biochemistry*. 57:255–257. https://doi.org/10.1021/acs.biochem.7b00845

Donati, A., I. Anselme, S. Schneider-Maunoury, and C. Vesque. 2021. Planar polarization of cilia in the zebrafish floor-plate involves Par3-mediated posterior localization of highly motile basal bodies. *Development*. 148:dev196386.https://doi.org/10.1242/dev.196386

Ear, J., A. Saklecha, N. Rajapakse, J. Choi, M. Ghassemian, I. Kufareva, and P. Ghosh. 2020. Tyrosine-based signals regulate the assembly of Daple-PARD3 complex at cell–cell junctions. *iScience*. 23:100859. https://doi.org/10.1016/j.isci.2020.100859

Furukawa, K.T., K. Yamashita, N. Sakurai, and S. Ohno. 2017. The epithelial circumferential actin belt regulates YAP/TAZ through nucleocytoplasmic shuttling of merlin. *Cell Rep.* 20:1435–1447. https://doi.org/10.1016/j.celrep.2017.07.032

Garcia-Marcos, M., P. Ghosh, and M.G. Farquhar. 2009. GIV is a nonreceptor GEF for G alpha i with a unique motif that regulates Akt signaling. *Proc. Natl. Acad. Sci. USA*. 106:3178–3183. https://doi.org/10.1073/pnas.0900294106

Garcia De Las Bayonas, A., J.M. Philippe, A.C. Lellouch, and T. Lecuit. 2019. Distinct RhoGEFs activate apical and junctional contractility under control of G proteins during epithelial morphogenesis. *Curr. Biol.* 29:3370–3385.e7. https://doi.org/10.1016/j.cub.2019.08.017

Ghosh, P., M. Garcia-Marcos, S.J. Bornheimer, and M.G. Farquhar. 2008. Activation of Galphai3 triggers cell migration via regulation of GIV. *J. Cell Biol.* 182:381–393. https://doi.org/10.1083/jcb.200712066

Gilmour, D., M. Rembold, and M. Leptin. 2017. From morphogen to morphogenesis and back. *Nature*. 541:311–320. https://doi.org/10.1038/nature21348

Harris, T.J., and M. Peifer. 2004. Adherens junction-dependent and -independent steps in the establishment of epithelial cell polarity in *Drosophila*. *J. Cell Biol.* 167:135–147. https://doi.org/10.1083/jcb.200406024

Horikoshi, Y., A. Suzuki, T. Yamanaka, K. Sasaki, K. Mizuno, H. Sawada, S. Yonemura, and S. Ohno. 2009. Interaction between PAR-3 and the aPKC-PAR-6 complex is indispensable for apical domain development of epithelial cells. *J. Cell Biol.* 122:1595–1606. https://doi.org/10.1242/jcs.043174

Ishida-Takagishi, M., A. Enomoto, N. Asai, K. Ushida, T. Watanabe, T. Hashimoto, T. Kato, L. Weng, S. Matsumoto, M. Asai, et al. 2012. The Dishevelled-associating protein Daple controls the non-canonical Wnt/Rac pathway and cell motility. *Nat. Commun.* 3:859. https://doi.org/10.1038/ncomms1861

Ishiuchi, T., and M. Takeichi. 2011. Willin and Par3 cooperatively regulate epithelial apical constriction through aPKC-mediated ROCK phosphorylation. *Nat. Cell Biol.* 13:860–866. https://doi.org/10.1038/ncb2274

Jha, A., T.S. van Zanten, J.M. Philippe, S. Mayor, and T. Lecuit. 2018. Quantitative control of GPCR organization and signaling by endocytosis in epithelial morphogenesis. *Curr. Biol.* 28:1570–1584.e6. https://doi.org/10.1016/j.cub.2018.03.068

Jia, C.Y., J. Nie, C. Wu, C. Li, and S.S. Li. 2005. Novel Src homology 3 domain-binding motifs identified from proteomic screen of a Pro-rich region. *Mol. Cell. Proteomics*. 4:1155–1166. https://doi.org/10.1074/mcp.M500108-MCP200

Johnson, R.I., M.J. Seppa, and R.L. Cagan. 2008. The *Drosophila* CD2AP/CIN85 orthologue Cindr regulates junctions and cytoskeleton dynamics during tissue patterning. *J. Cell Biol.* 180:1191–1204. https://doi.org/10.1083/jcb.200706108

Kanesaki, T., S. Hirose, J. Grosshans, and N. Fuse. 2013. Heterotrimeric G protein signaling governs the cortical stability during apical constriction in *Drosophila* gastrulation. *Mech. Dev.* 130:132–142. https://doi.org/10.1016/j.mod.2012.10.001

Kannan, N., and V.W. Tang. 2018. Myosin-1c promotes E-cadherin tension and force-dependent recruitment of α-actinin to the epithelial cell junction. *J. Cell Sci.* 131:jcs211334.

Kerridge, S., A. Munjal, J.M. Philippe, A. Jha, A.G. de las Bayonas, A.J. Saurin, and T. Lecuit. 2016. Modular activation of Rho1 by GPCR signalling imparts polarized myosin II activation during morphogenesis. *Nat. Cell Biol.* 18:261–270. https://doi.org/10.1038/ncb3302

Kim, H.Y., T.R. Jackson, C. Stuckenholz, and L.A. Davidson. 2020. Tissue mechanics drives regeneration of a mucociliated epidermis on the surface of Xenopus embryonic aggregates. *Nat. Commun.* 11:665. https://doi.org/10.1038/s41467-020

Kirsch, K.H., M.M. Georgescu, S. Ishimaru, and H. Hanafusa. 1999. CMS: An adapter molecule involved in cytoskeletal rearrangements. *Proc. Natl. Acad. Sci. USA*. 96:6211–6216. https://doi.org/10.1073/pnas.96.11.6211

Kobayashi, H., T. Michiue, A. Yukita, H. Danno, K. Sakurai, A. Fukui, A. Kikuchi, and M. Asashima. 2005. Novel Daple-like protein positively regulates both the Wnt/beta-catenin pathway and the Wnt/JNK pathway in Xenopus. *Mech. Dev.* 122:1138–1153. https://doi.org/10.1016/j.mod.2005.05.003

Kuchinke, U., F. Grawe, and E. Knust. 1998. Control of spindle orientation in *Drosophila* by the Par-3-related PDZ-domain protein Bazooka. *Curr. Biol.* 8:1357–1365. https://doi.org/10.1016/s0960-9822(98)00016-5

Landin Malt, A., Z. Dailey, J. Holbrook-Rasmussen, Y. Zheng, A. Hogan, Q. Du, and X. Lu. 2019. Par3 is essential for the establishment of planar cell polarity of inner ear hair cells. *Proc. Natl. Acad. Sci. USA*. 116:4999–5008. https://doi.org/10.1073/pnas.1816333116

Landin Malt, A., A.K. Hogan, C.D. Smith, M.S. Madani, and X. Lu. 2020. Wnts regulate planar cell polarity via heterotrimeric G protein and PI3K signaling. *J. Cell Biol.* 219:e201912071. https://doi.org/10.1083/jcb.201912071

Lecuit, T., P.F. Lenne, and E. Munro. 2011. Force generation, transmission, and integration during cell and tissue morphogenesis. *Annu. Rev. Cell Dev. Biol.* 27:157–184. https://doi.org/10.1146/annurev-cellbio-100109-104027

Lecuit, T., and A.S. Yap. 2015. E-cadherin junctions as active mechanical integrators in tissue dynamics. *Nat. Cell Biol.* 17:533–539. https://doi.org/10.1038/ncb3136

Lin, D., A.S. Edwards, J.P. Fawcett, G. Mbamalu, J.D. Scott, and T. Pawson. 2000. A mammalian PAR-3-PAR-6 complex implicated in Cdc42/Rac1 and aPKC signalling and cell polarity. *Nat. Cell Biol.* 2:540–547. https://doi.org/10.1038/35019582

Mahuzier, A., A. Shihavuddin, C. Fournier, P. Lansade, M. Faucourt, N. Menezes, A. Meunier, M. Garfa-Traore, M.F. Carlier, R. Voituriez, et al. 2018. Ependymal cilia beating induces an actin network to protect centrioles against shear stress. *Nat. Commun.* 9:2279. https://doi.org/10.1038/s41467-018

Manning, A.J., K.A. Peters, M. Peifer, and S.L. Rogers. 2013. Regulation of epithelial morphogenesis by the G protein-coupled receptor mist and its ligand fog. *Sci. Signal.* 6:ra98. https://doi.org/10.1126/scisignal.2004427

Manning, A.J., and S.L. Rogers. 2014. The fog signaling pathway: Insights into signaling in morphogenesis. *Dev. Biol.* 394:6–14. https://doi.org/10.1016/j.ydbio.2014.08.003

Marchiando, A.M., W.V. Graham, and J.R. Turner. 2010. Epithelial barriers in homeostasis and disease. *Annu. Rev. Pathol.* 5:119–144. https://doi.org/10.1146/annurev.pathol.4.110807.092135

Marivin, A., and M. Garcia-Marcos. 2019. DAPLE and MPDZ bind to each other and cooperate to promote apical cell constriction. *Mol. Biol. Cell*. 30:1900–1910. https://doi.org/10.1091/mbc.E19-02-0091

Marivin, A., M. Maziarz, J. Zhao, V. DiGiacomo, I. Olmos Calvo, E.A. Mann, J. Ear, J.B. Blanco-Canosa, E.M. Ross, P. Ghosh, and M. Garcia-Marcos. 2020. DAPLE protein inhibits nucleotide exchange on Gαs and Gαq via the same motif that activates Gαi. *J. Biol. Chem.* https://doi.org/10.1074/jbc.ra119.011648

Marivin, A., V. Morozova, I. Walawalkar, A. Leyme, D.A. Kretov, D. Cifuentes, I. Dominguez, and M. Garcia-Marcos. 2019. GPCR-independent activation of G proteins promotes apical cell constriction in vivo. *J. Cell Biol.* 218:1743–1763. https://doi.org/10.1083/jcb.201811174

Mizuno, K., A. Suzuki, T. Hirose, K. Kitamura, K. Kutsuzawa, M. Futaki, Y. Amano, and S. Ohno. 2003. Self-association of PAR-3-mediated by the conserved N-terminal domain contributes to the development of epithelial tight junctions. *J. Biol. Chem.* 278:31240–31250. https://doi.org/10.1074/jbc.m303593200

Moncalian, G., N. Cardenes, Y.L. Deribe, M. Spinola-Amilibia, I. Dikic, and J. Bravo. 2006. Atypical polyproline recognition by the CMS N-terminal Src homology 3 domain. *J. Biol. Chem.* 281:38845–38853. https://doi.org/10.1074/jbc.M606411200

Morais-de-Sa, E., V. Mirouse, and D. St Johnston. 2010. aPKC phosphorylation of Bazooka defines the apical/lateral border in *Drosophila* epithelial cells. *Cell*. 141:509–523. https://doi.org/10.1016/j.cell.2010.02.040

Muller, H.A., and E. Wieschaus. 1996. armadillo, bazooka, and stardust are critical for early stages in formation of the zonula adherens and maintenance of the polarized blastoderm epithelium in *Drosophila*. *J. Cell Biol.* 134:149–163. https://doi.org/10.1083/jcb.134.1.149

Nagai-Tamai, Y., K. Mizuno, T. Hirose, A. Suzuki, and S. Ohno. 2002. Regulated protein-protein interaction between aPKC and PAR-3 plays an essential role in the polarization of epithelial cells. *Gene Cell.* 7:1161–1171. https://doi.org/10.1046/j.1365-2443.2002.00590.x

Nakajima, H., and T. Tanoue. 2011. Lulu2 regulates the circumferential actomyosin tensile system in epithelial cells through p114RhoGEF. *J. Cell Biol.* 195:245–261. https://doi.org/10.1083/jcb.201104118

Nakayama, S., T. Yano, T. Namba, S. Konishi, M. Takagishi, E. Herawati, T. Nishida, Y. Imoto, S. Ishihara, M. Takahashi, et al. 2021. Planar cell polarity induces local microtubule bundling for coordinated ciliary beating. *J. Cell Biol.* 220:e202010034. https://doi.org/10.1083/jcb.202010034

Nance, J., and J.A. Zallen. 2011. Elaborating polarity: PAR proteins and the cytoskeleton. *Development*. 138:799–809. https://doi.org/10.1242/dev.053538

Newport, J., and M. Kirschner. 1982. A major developmental transition in early Xenopus embryos: II. Control of the onset of transcription. *Cell*. 30:687–696. https://doi.org/10.1016/0092-8674(82)90273-2

Oshita, A., S. Kishida, H. Kobayashi, T. Michiue, T. Asahara, M. Asashima, and A. Kikuchi. 2003. Identification and characterization of a novel Dvl-binding protein that suppresses Wnt signalling pathway. *Genes Cell.* 8:1005–1017. https://doi.org/10.1111/j.1365-2443.2003.00692.x

Ossipova, O., K. Kim, B.B. Lake, K. Itoh, A. Ioannou, and S.Y. Sokol. 2014. Role of Rab11 in planar cell polarity and apical constriction during vertebrate neural tube closure. *Nat. Commun.* 5:3734. https://doi.org/10.1038/ncomms4734

Park, T.J., B.J. Mitchell, P.B. Abitua, C. Kintner, and J.B. Wallingford. 2008. Dishevelled controls apical docking and planar polarization of basal bodies in ciliated epithelial cells. *Nat. Genet.* 40:871–879. https://doi.org/10.1038/ng.104

Parks, S., and E. Wieschaus. 1991. The *Drosophila* gastrulation gene concertina encodes a G alpha-like protein. *Cell*. 64:447–458. https://doi.org/10.1016/0092-8674(91)90652-f

Peterson, L.J., Z. Rajfur, A.S. Maddox, C.D. Freel, Y. Chen, M. Edlund, C. Otey, and K. Burridge. 2004. Simultaneous stretching and contraction of stress fibers in vivo. *Mol. Biol. Cell*. 15:3497–3508. https://doi.org/10.1091/mbc.e03-09-0696

Piekny, A.J., and M. Glotzer. 2008. Anillin is a scaffold protein that links RhoA, actin, and myosin during cytokinesis. *Curr. Biol.* 18:30–36. https://doi.org/10.1016/j.cub.2007.11.068

Priya, R., G.A. Gomez, S. Budnar, S. Verma, H.L. Cox, N.A. Hamilton, and A.S. Yap. 2015. Feedback regulation through myosin II confers robustness on RhoA signalling at E-cadherin junctions. *Nat. Cell Biol.* 17:1282–1293. https://doi.org/10.1038/ncb3239

Ratheesh, A., G.A. Gomez, R. Priya, S. Verma, E.M. Kovacs, K. Jiang, N.H. Brown, A. Akhmanova, S.J. Stehbens, and A.S. Yap. 2012. Centralspindlin and alpha-catenin regulate Rho signalling at the epithelial zonula adherens. *Nat. Cell Biol.* 14:818–828. https://doi.org/10.1038/ncb2532

Rodriguez-Boulan, E., and I.G. Macara. 2014. Organization and execution of the epithelial polarity programme. *Nat. Rev. Mol. Cell Biol.* 15:225–242. https://doi.org/10.1038/nrm3775

Rouka, E., P.C. Simister, M. Janning, J. Kumbrink, T. Konstantinou, J.R. Muniz, D. Joshi, N. O'Reilly, R. Volkmer, B. Ritter, et al. 2015. Differential recognition preferences of the three Src homology 3 (SH3) domains from the adaptor CD2-associated protein (CD2AP) and direct association with Ras and Rab interactor 3 (RIN3). *J. Biol. Chem.* 290: 25275–25292. https://doi.org/10.1074/jbc.m115.637207

Sfakianos, J., A. Togawa, S. Maday, M. Hull, M. Pypaert, L. Cantley, D. Toomre, and I. Mellman. 2007. Par3 functions in the biogenesis of the primary cilium in polarized epithelial cells. *J. Cell Biol.* 179:1133–1140. https://doi.org/10.1083/jcb.200709111

Siedlik, M.J., and C.M. Nelson. 2015. Regulation of tissue morphodynamics: An important role for actomyosin contractility. *Curr. Opin. Genet. Dev.* 32:80–85. https://doi.org/10.1016/j.gde.2015.01.002

Silver, J.T., F. Wirtz-Peitz, S. Simoes, M. Pellikka, D. Yan, R. Binari, T. Nishimura, Y. Li, T.J.C. Harris, N. Perrimon, and U. Tepass. 2019. Apical polarity proteins recruit the RhoGEF Cysts to promote junctional myosin assembly. *J. Cell Biol.* 218:3397–3414. https://doi.org/10.1083/jcb.201807106

Stols, L., M. Gu, L. Dieckman, R. Raffen, F.R. Collart, and M.I. Donnelly. 2002. A new vector for high-throughput, ligation-independent cloning encoding a tobacco etch virus protease cleavage site. *Protein Expr. Purif.* 25: 8–15. https://doi.org/10.1006/prep.2001.1603

Suzuki, A., and S. Ohno. 2006. The PAR-aPKC system: Lessons in polarity. *J. Cell Sci.* 119:979–987. https://doi.org/10.1242/jcs.02898

Suzuki, A., T. Yamanaka, T. Hirose, N. Manabe, K. Mizuno, M. Shimizu, K. Akimoto, Y. Izumi, T. Ohnishi, and S. Ohno. 2001. Atypical protein kinase C is involved in the evolutionarily conserved par protein complex and plays a critical role in establishing epithelia-specific junctional structures. *J. Cell Biol.* 152:1183–1196. https://doi.org/10.1083/jcb.152.6.1183

Takagishi, M., N. Esaki, K. Takahashi, and M. Takahashi. 2020. Cytoplasmic dynein functions in planar polarization of basal bodies within ciliated cells. *iScience*. 23:101213. https://doi.org/10.1016/j.isci.2020.101213

Takagishi, M., M. Sawada, S. Ohata, N. Asai, A. Enomoto, K. Takahashi, L. Weng, K. Ushida, H. Ara, S. Matsui, et al. 2017. Daple coordinates planar polarized microtubule dynamics in ependymal cells and contributes to hydrocephalus. *Cell Rep.* 20:960–972. https://doi.org/10.1016/j.celrep.2017.06.089

Takeichi, M. 2014. Dynamic contacts: Rearranging adherens junctions to drive epithelial remodelling. *Nat. Rev. Mol. Cell Biol.* 15:397–410. https://doi.org/10.1038/nrm3802

Tang, V.W. 2018. Cell–cell adhesion interface: Orthogonal and parallel forces from contraction, protrusion, and retraction. *F1000Res.* 7:F1000

Tang, V.W., and W.M. Brieher. 2013. FSGS3/CD2AP is a barbed-end capping protein that stabilizes actin and strengthens adherens junctions. *J. Cell Biol.* 203:815–833. https://doi.org/10.1083/jcb.201304143

Tateishi, K., T. Nishida, K. Inoue, and S. Tsukita. 2017. Three-dimensional organization of layered apical cytoskeletal networks associated with mouse airway tissue development. *Sci. Rep.* 7:43783. https://doi.org/10.1038/srep43783

Terry, S.J., C. Zihni, A. Elbediwy, E. Vitiello, I.V. Leefa Chong San, M.S. Balda, and K. Matter. 2011. Spatially restricted activation of RhoA signalling at epithelial junctions by p114RhoGEF drives junction formation and morphogenesis. *Nat. Cell Biol.* 13:159–166. https://doi.org/10.1038/ncb2156

Wang, Y., and W.M. Brieher. 2020. CD2AP links actin to PI3 kinase activity to extend epithelial cell height and constrain cell area. *J. Cell Biol.* 219: e201812087. https://doi.org/10.1083/jcb.201812087

Werner, M.E., P. Hwang, F. Huisman, P. Taborek, C.C. Yu, and B.J. Mitchell. 2011. Actin and microtubules drive differential aspects of planar cell polarity in multiciliated cells. *J. Cell Biol.* 195:19–26. https://doi.org/10.1083/jcb.201106110

Werner, M.E., and B.J. Mitchell. 2013. Using Xenopus skin to study cilia development and function. *Methods Enzymol.* 525:191–217. https://doi.org/10.1016/B978-012-397944-5.00010-9

Yano, T., H. Kanoh, A. Tamura, and S. Tsukita. 2017. Apical cytoskeletons and junctional complexes as a combined system in epithelial cell sheets. *Ann. N.Y Acad. Sci.* 1405:32–43. https://doi.org/10.1111/nyas.13432

Yu, H.H., and J.A. Zallen. 2020. Abl and Canoe/Afadin mediate mechanotransduction at tricellular junctions. *Science*. 370:eaba5528. https://doi.org/10.1126/science.aba5528

Zallen, J.A., and E. Wieschaus. 2004. Patterned gene expression directs bipolar planar polarity in *Drosophila*. *Dev. Cell*. 6:343–355. https://doi.org/10.1016/s1534-5807(04)00060-7

Zihni, C., C. Mills, K. Matter, and M.S. Balda. 2016. Tight junctions: From simple barriers to multifunctional molecular gates. *Nat. Rev. Mol. Cell Biol.* 17:564–580. https://doi.org/10.1038/nrm.2016.80

Supplemental material

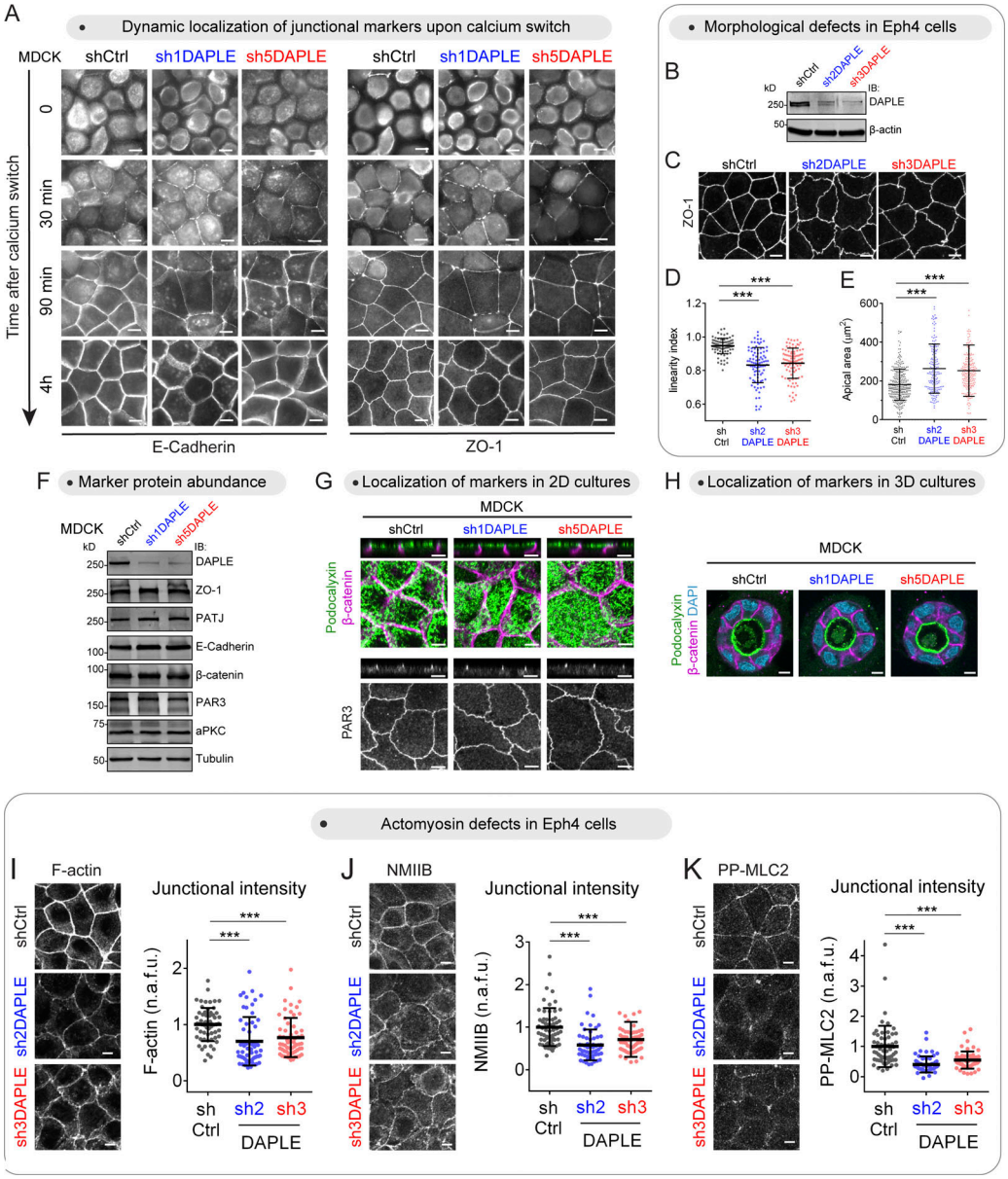

Figure S1. **Loss of DAPLE impairs junctional morphology and actomyosin without altering the localization or abundance of junctional and apicobasal polarity markers. (A)** Loss of DAPLE does not alter the formation of cell–cell junctions upon calcium-switch. MDCK cell monolayers seeded on filters were incubated for 18 h in medium with reduced Ca^{2+}, and assembly of cell–cell junctions was induced by switching cells to medium containing Ca^{2+} for the indicated times. Cells stained for E-Cadherin and ZO-1, as indicated, were imaged by wide-field fluorescence microcopy. Representative pictures from three independent experiments are shown. **(B–E)** Loss of DAPLE alters cell–cell junction morphology in Eph4 cells. Eph4 cells stably expressing shCtrl (control), sh2DAPLE, or sh3DAPLE RNAi sequences were generated by lentiviral transduction and lysed for IB with the indicated antibodies (B). Confocal fluorescence microscopy images of ZO-1–stained Eph4 cells (C) were used to determine apical cell–cell junction linearity (D) or apical areas (E). Scatter plot values are for 90 cell–cell junctions (three experiments) in (D) or cells from 12 fields (three experiments) in E. Mean ± SD; ***, $P < 0.001$, Mann–Whitney *U* test. **(F)** Loss of DAPLE does not affect the total amount of junctional proteins. Monolayers of the MDCK cell lines (shCtrl, sh1DAPLE, or sh5DAPLE) were analyzed by IB as indicated. Representative results of two independent experiments are shown. **(G)** Loss of DAPLE does not perturb the localization of markers of apicobasal polarity in 2D cell cultures. Monolayers of the indicated MDCK cell lines (shCtrl, sh1DAPLE, or sh5DAPLE) were costained for Podocalyxin (apical membranes) and β-catenin (lateral membranes) or stained for PAR3 (apical junctions) and imaged by confocal fluorescence microscopy. For each staining, upper panels are perpendicular optical cross-sections, and lower panels are top views corresponding to maximum-intensity projections for Podocalyxin/β-catenin, or a single optical section for PAR3. Representative pictures from two experiments are shown. **(H)** Loss of DAPLE does not perturb the localization of markers of apicobasal polarity in 3D cell cultures. Cysts of the indicated MDCK cell lines (shCtrl, sh1DAPLE, or sh5DAPLE) were grown on Matrigel and costained for Podocalyxin and β-catenin before analysis by fluorescence confocal microscopy. Representative single optical sections of two independent experiments are shown. **(I–K)** Loss of DAPLE in Eph4 cells decreases the levels of junctional F-actin, NMIIB, and PP-MLC2. Monolayers of the indicated Eph4 cell lines (shCtrl, sh2DAPLE, or sh3DAPLE) were stained for F-actin (I), NMIIB (J), or PP-MLC2 (K) and analyzed by confocal fluorescence microscopy. Each panel depicts maximum-intensity projections of the apical domain (0.7 µm) and quantification graphs of fluorescence intensity at apical cell–cell junctions (scatter plots with mean ± SD for ∼60 cell–cell boundaries from three independent experiments; ***, $P < 0.001$, Mann–Whitney *U* test). All scale bars are 5 µm. Source data are available for this figure: SourceData FS1.

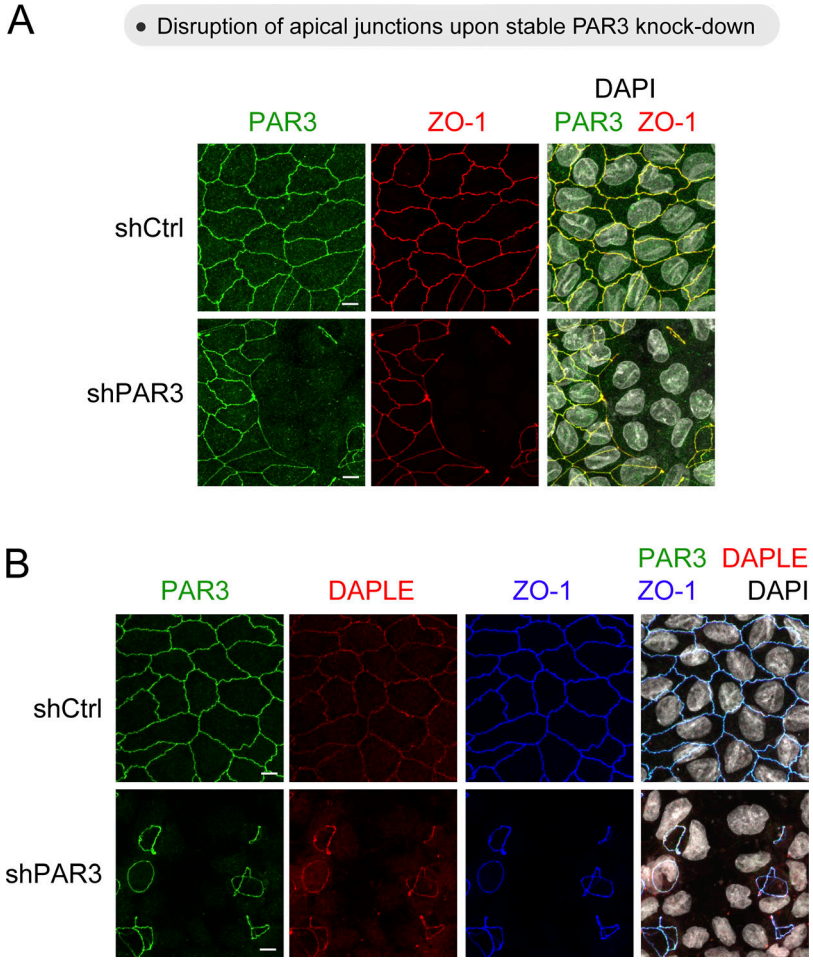

Figure S2. **MDCK cells stably depleted of PAR3 display disrupted apical cell junctions. (A and B)** Established MDCK cell monolayers stably expressing shCtrl (control) or shPAR3 (shPAR3) were stained for PAR3, ZO-1, and DAPLE, as indicated, and imaged by confocal fluorescence microscopy. Representative images of maximum-intensity projections (top view) from three or more independent experiments are shown.

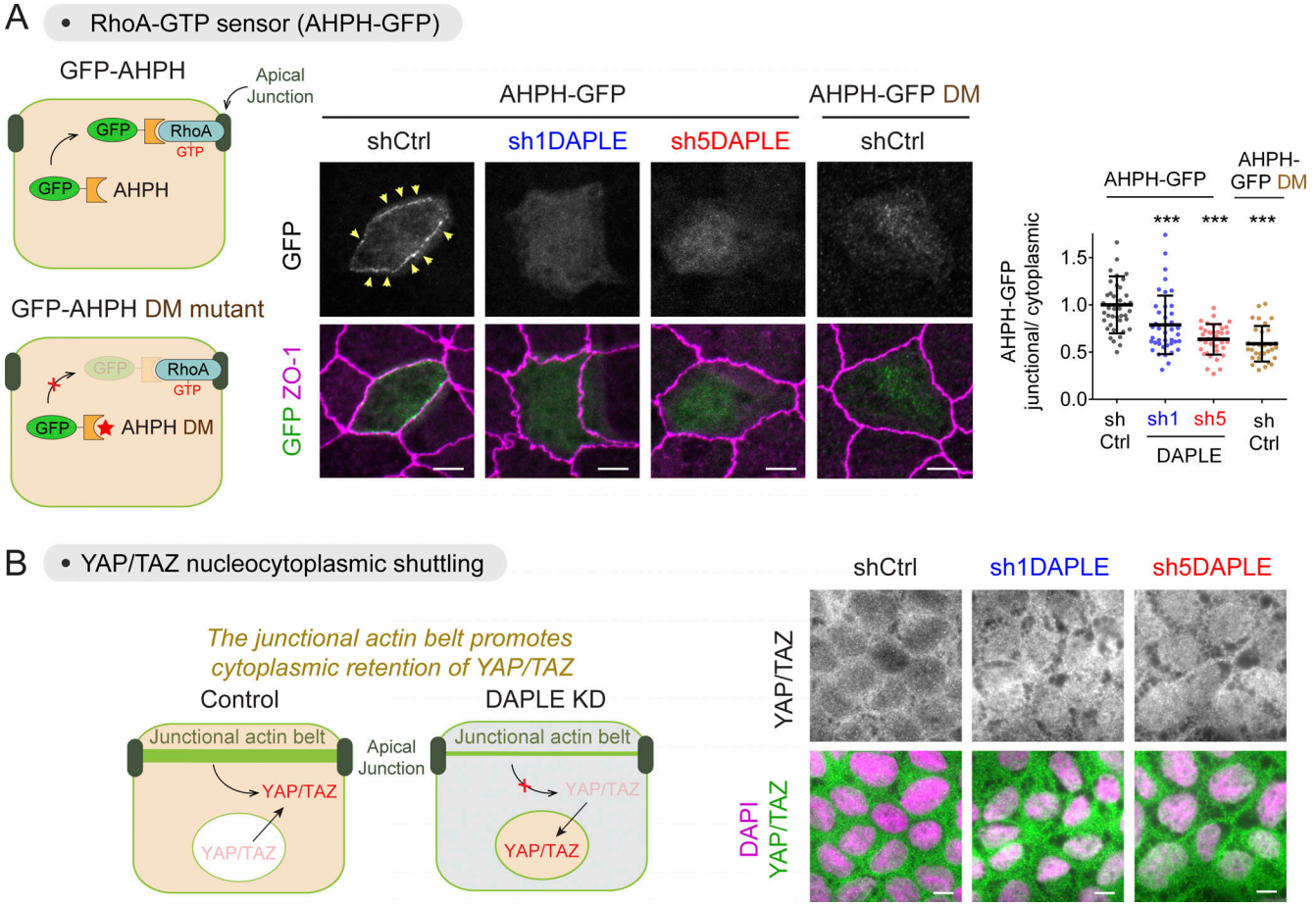

Figure S3. **Loss of DAPLE decreases RhoA-GTP levels at apical cell junctions and favors YAP/TAZ nuclear localization. (A)** Loss of DAPLE decreases RhoA-GTP levels at apical cell junctions. The indicated MDCK cell lines (shCtrl, sh1DAPLE, or sh5DAPLE) were transfected with AHPH-GFP plasmids, stained for ZO-1 and GFP, and analyzed by confocal fluorescence microscopy. Images correspond to maximum-intensity projection of the apical domain, and graphs are the quantification of GFP fluorescence intensities at junctions (scatter plot with mean ± SD for 30–40 cell–cell boundaries from four independent experiments; ***, $P < 0.001$ compared with shCtrl, Mann–Whitney *U* test). **(B)** Loss of DAPLE promotes the nuclear localization of YAP/TAZ. The indicated MDCK cell lines (shCtrl, sh1DAPLE, or sh5DAPLE) were stained for YAP/TAZ and analyzed by wide-field fluorescence microscopy. Images are representative results from three independent experiments. All scale bars are 5 µm.

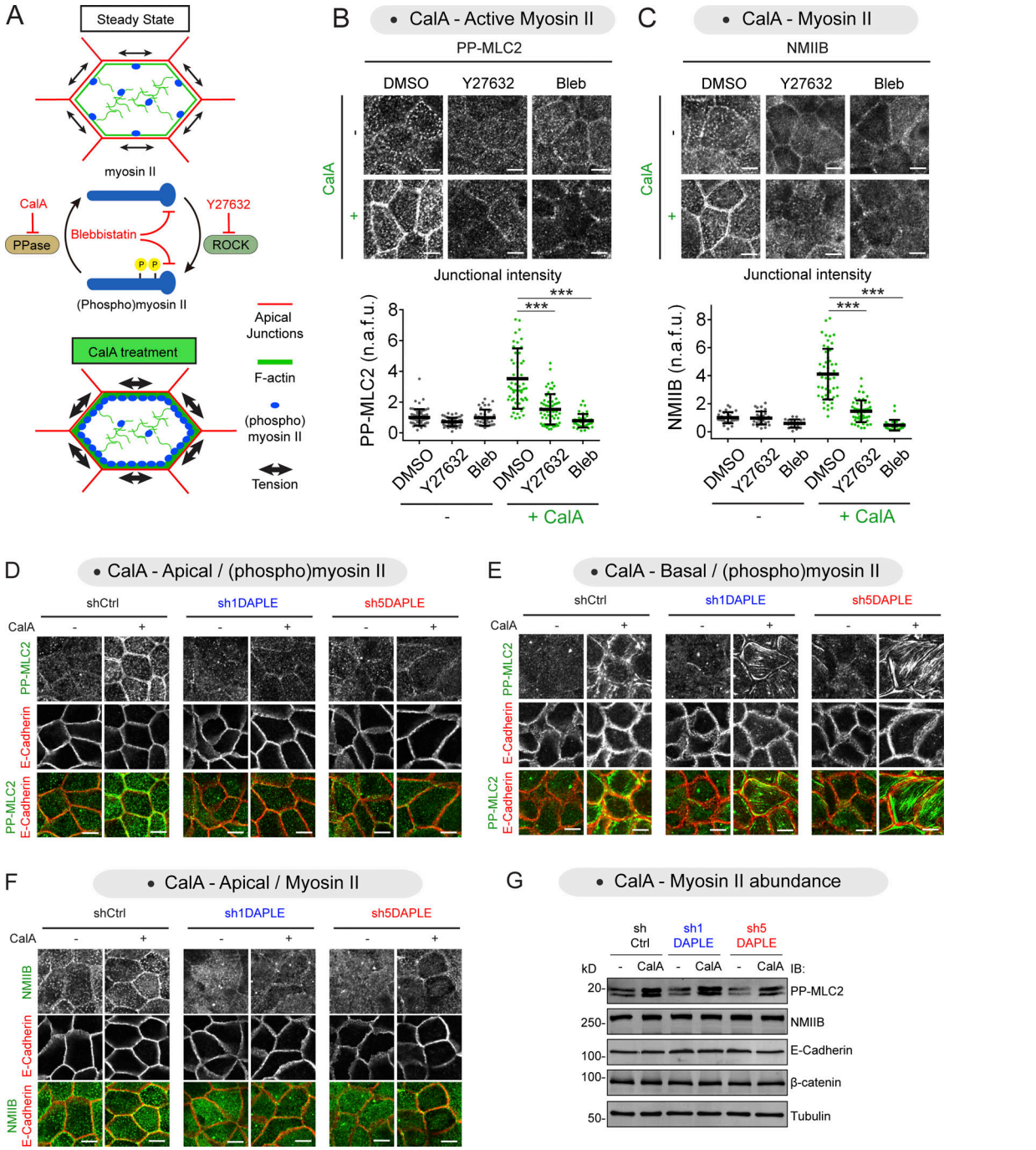

Figure S4. **Loss of DAPLE impairs CalA-induced accumulation of active myosin II at apical cell junctions. (A)** Diagram depicting CalA-induced apical accumulation of active myosin II that depends on ROCK and myosin II activity. CalA inhibits myosin phosphatases (PPase), which favors the accumulation of active phosphorylated myosin II. In contrast, the ROCK inhibitor Y27632 and the myosin inhibitor blebbistatin impair myosin activation. **(B and C)** Y27632 and blebbistatin prevent the accumulation of junctional PP-MLC2 (B) or NMIIB (C) upon CalA treatment. MDCK cells were preincubated with Y27632 (10 µM, 30 min), blebbistatin (Bleb, 50 µM, 60 min), or an equivalent volume of DMSO before CalA treatments (80 nM, 20 min). Images on the top of each panel correspond to representative single optical sections at the level of apical junctions, and quantification graphs of junctional intensities of PP-MLC2 (B) or NMIIB (C) are shown on the bottom of each panel (scatter plots with mean ± SD for ∼60 cell–cell boundaries from three independent experiments; ***, P < 0.001, Mann–Whitney *U* test). **(D and E)** Loss of DAPLE prevents the accumulation of apical, but not basal, PP-MLC2 upon CalA treatment. MDCK cell lines were treated with CalA as indicated, stained for PP-MLC2 and E-cadherin, and analyzed by confocal fluorescence microscopy. Representative single optical sections of the same fields of cells either at the level of apical junctions or at the level of the basal membrane are shown in D or E, respectively. The images for apical PP-MLC2 are the same as in Fig. 3 F. **(F)** Loss of DAPLE prevents the accumulation of apical NMIIB upon CalA treatment. The same images as shown in Fig. 3 G for NMIIB are displayed here along with E-cadherin costaining to clearly delimit the boundaries of cell–cell junctions for all conditions. **(G)** Loss of DAPLE does not alter the total cellular amount of PP-MLC2, NMIIB, or junctional proteins with or without CalA treatment. The indicated MDCK cell lines treated or not with CalA as in B and C were lysed and analyzed by IB as indicated. Representative results of two independent experiments are shown. All scale bars are 5 µm. Source data are available for this figure: SourceData FS4.

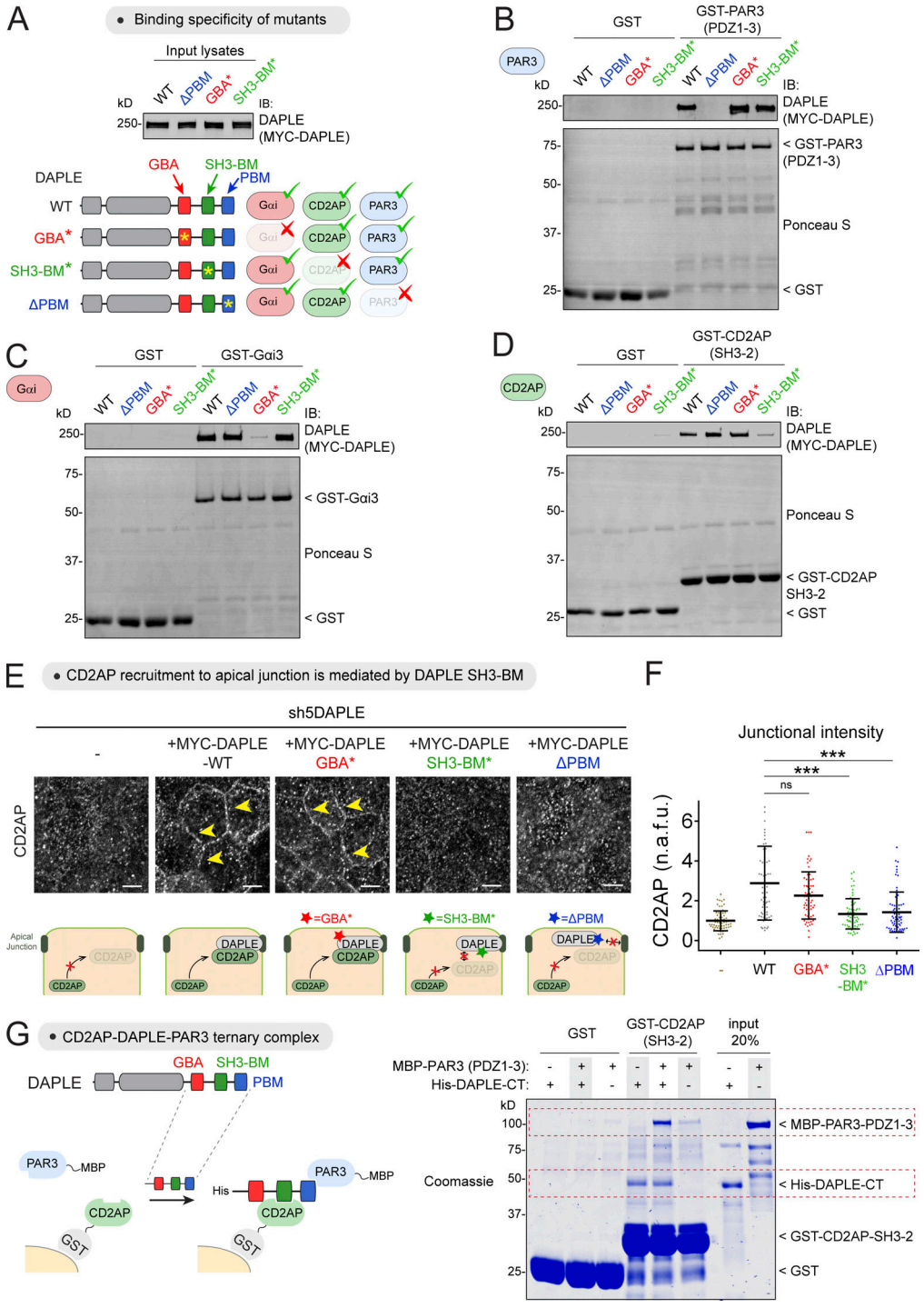

Figure S5. **Assessment of modular interactions of DAPLE with CD2AP and PAR3. (A)** Lysates of HEK293T cells transfected with MYC-DAPLE WT, ΔPBM, GBA*, or SH3-BM* used as the source of soluble ligands for the GST pull-down experiments presented in this figure. Diagram depicts the expected results if the mutations disrupt the cognate interaction specifically. **(B)** DAPLE ΔPBM, but not GBA* or SH3-BM*, mutant disrupts binding to PAR3. **(C)** DAPLE GBA*, but not ΔPBM or SH3-BM*, mutant disrupts binding to Gαi3. **(D)** DAPLE SH3-BM*, but not ΔPBM or GBA*, mutant disrupts binding to CD2AP. Lysates of HEK293T cells transfected with the indicated MYC-DAPLE constructs were incubated with GST, GST-PAR3 (PDZ1-3), GST-Gαi3, or GST-CD2AP (SH3-2), as indicated in each panel, immobilized on glutathione-agarose beads. Bead-bound proteins were detected by Ponceau S staining or IB. Results in B–D are representative of three independent experiments. **(E and F)** MYC-DAPLE WT, GBA*, SH3-BM*, or ΔPBM were stably expressed in DAPLE-depleted MDCK cells (sh5DAPLE) by lentiviral transduction, and cells were stained for CD2AP. Representative pictures of maximum-intensity projection of the apical domain (1 µm) are shown in A, and quantification of junctional intensities for CD2AP is shown in B represented as a scatter plot with mean ± SD for ∼60 cell–cell boundaries from three independent experiments; ***, P < 0.001, Mann–Whitney *U* test. Scale bars are 5 µm. **(G)** Formation of a ternary complex between CD2AP, DAPLE, and PAR3. Purified His-DAPLE-CT and MBP-PAR3 (PDZ1-3) were incubated with GST or GST-CD2AP (SH3-2), as indicated, immobilized on glutathione-agarose beads. Bead-bound proteins were detected by Coomassie staining. Results are representative of three independent experiments. Source data are available for this figure: SourceData FS5.